Effective global mixing of the highly siderophile elements into Earth's mantle inferred from oceanic abyssal peridotites

Marine Paquet, James M.D. Day, Diana B Brown, Christopher L Waters

Effective global mixing of the highly siderophile elements into Earth's mantle inferred from oceanic abyssal peridotites

Marine Paquet[1,2], James M.D. Day[1], Diana B. Brown[1], Christopher L. Waters[1]

[1]*Scripps Institution of Oceanography, University of California San Diego, La Jolla, CA 92093, USA (mpaquet@ucsd.edu, jmdday@ucsd.edu)*

[2]*Institut de Physique du Globe de Paris, UMR 7154 CNRS, Université de Paris, 1 rue Jussieu, 75238 Paris, France*

Manuscript Statistics

Abstract: 407 words

Main Text: 6689 words

Figures: 8 (+6 supplementary figures)

Tables: 1 (+7 supplementary tables)

Keywords: Oceanic mantle; peridotite; highly siderophile elements; Os isotopes; late accretion; mantle convection; heterogeneity

ABSTRACT

Late accretion occurred through addition of massive impactors to Earth, leading to potential heterogeneities in the distribution of highly siderophile elements (HSE: Os, Ir, Ru, Pt, Pd, Re) within the mantle. Abyssal peridotites sample the present-day convecting mantle, which make them useful for examining the distribution of the HSE within the mantle. Here we report new HSE abundance data and $^{187}Os/^{188}Os$ ratios, in conjunction with mineral chemistry and bulk rock major- and trace-element compositions for abyssal peridotites from the fast-spreading Pacific Antarctic Ridge (PAR) and East Pacific Rise (Hess Deep), and for slow to intermediate spreading ridges from the Southwest Indian Ridge, Central Indian Ridge and Mid Atlantic Ridge. These analyses expand the global abyssal peridotite Os isotope and HSE database, enabling evaluation of potential variations with spreading rate, from ultraslow (<20 mm, full spreading rate) to fast (135-150 mm/yr). Accounting for likely effects from seawater modification and serpentinization, the Pacific data reveals heterogeneous and sometimes significant melt depletion for PAR (3-23% melt depletion; $^{187}Os/^{188}Os$ from 0.1189 to 0.1336, average = 0.1267±0.0065; 2SD) and Hess Deep abyssal peridotites (15-20% melt depletion; 0.1247±0.0027). Abyssal peridotites from fast to intermediate spreading ridges reveal no systematic differences in the distribution and behavior of the HSE or Os isotopes, or in degrees of melt depletion, compared with slow to ultraslow spreading ridges. These observations arise despite significant differences in melt generation processes at mid-ocean ridges suggesting that the effects of ancient melt depletion are more profound on HSE compositions in abyssal peridotites than modern melting beneath ridges. Using global abyssal peridotites with Al_2O_3 content > 2 wt.%, the average composition of the primitive mantle is 0.3 ppb Re, 4.9 ppb Pd, 7.1 ppb Pt, 7.2 ppb Ru, 3.8 ppb Ir and Os, showing no Pd/Ir, but a positive Ru/Ir anomaly, relative to chondrites. There is ~50% variation of the HSE abundances in the oceanic mantle, with much of this variation being observed at small length scales (<1 km) and due entirely to both modern and more ancient partial melting effects. Consequently, any significant HSE heterogeneities formed during late accretion or early Earth differentiation processes are no longer recognizable in the mantle sampled within ocean basins, implying generally efficient mixing of Earth's mantle for these elements. By contrast, relatively ancient heterogeneity in Os and other radiogenic isotopes has been effectively preserved in the convecting mantle over the last ~2 Ga, through recycling processes and through preservation and isolation of melt-depleted refractory residues.

1. INTRODUCTION

The highly siderophile elements (HSE: Os, Ir, Ru, Pt, Rh, Pd, Re, Au) are key geochemical tools with which to investigate terrestrial accretion and differentiation processes. The HSE are generally compatible during partial melting and are characterized by elevated metal-silicate partition coefficients at mantle pressures (> 10^4; e.g., O'Neill et al., 1995; Holzheid et al., 2000; Ertel et al., 2001; Brenan and McDonough, 2009; Brenan et al., 2016; Suer et al., 2021 and references therein). Assuming such high partition coefficients, Earth's core and mantle are not in equilibrium for the HSE, and the mantle has abundances of these elements only ~150 times less abundant than in chondrites; some three orders of magnitude higher than expected (Morgan, 1986; Snow and Schmidt, 1998; Morgan et al., 2001; Becker et al., 2006; Fischer-Gödde et al., 2011; Day et al., 2016a; 2017a).

Three main hypotheses have been suggested to explain this discrepancy: (1) the "late accretion" or "late veneer" hypothesis where addition of "chondritic" impactors occurred after the major phase(s) of core formation (e.g., Turekian and Clark, 1969; Kimura et al., 1974; Chou, 1978; Jagoutz et al., 1979; Wänke, 1981; Meisel et al., 1996); (2) mixing or inefficient separation of differentiated outer-core material back into the mantle shortly after core separation (Jones & Drake, 1986; Snow & Schmidt, 1998), or; (3) lower metal-silicate partition coefficients at higher pressures and temperatures (HP-HT; e.g., Ringwood, 1977; Murthy, 1991). The late accretion model is generally the most popular given its ability to explain both the broadly chondritic $^{187}Os/^{188}Os$ as well as the elevated absolute abundances of the HSE that are in chondritic proportions within the bulk silicate Earth (BSE), requiring between ~0.5 and 0.8 wt.% addition of mass to Earth (Becker et al., 2006; Day et al., 2016a).

An outstanding question that remains, however, is how evenly distributed the HSE are within the present-day convecting mantle. Late accretion likely occurred through addition of massive impactors (Bottke et al., 2010), leading to the possibility of heterogeneous distribution of the HSE within Earth's mantle following late accretionary impacts, and enhanced deposition of impactor material within the mantle, perhaps at hemispheric scales, or at the scale of thousands of kilometers. For example, it has been demonstrated that metal-silicate equilibration differs depending on the target latitude of the impactor due to the influence of the planetary rotation on the mixing and settling history, which may generate chemical heterogeneities (e.g., HSE) and isotopic anomalies (e.g., ^{182}W anomalies) (Maas et al., 2021). For smaller planetary bodies, such as the probable asteroidal source of eucrite and diogenite meteorites, 4-Vesta, it has been proposed that the inferred patchy distribution of the HSE reflects regional rather than global late accretion effects shortly after planet formation (Day et al., 2012). In contrast, while Earth may have originally had a more heterogeneous distribution of the HSE within the mantle, compositional variations in mantle materials at the present-day are seemingly more consistent with homogeneous distributions through prolonged melting and/or solid-state convection. The evidence from mantle peridotites preserved in ophiolites is that there is more limited heterogeneity at >km length scales than at the scale of meters or less (e.g., O'Driscoll et al., 2012; Snortum & Day, 2020; Haller et al., 2021). Arguably, however, the ideal test of HSE homogeneity in Earth's mantle comes from the study of oceanic abyssal peridotites. Abyssal peridotites are samples of Earth's present-day convecting mantle sampled within ocean basins, so provide a snap-shot of the degree of present-day HSE homogeneity within the mantle.

Prior attempts to estimate the HSE composition of Earth's mantle have assumed relative initial homogeneity to attain a BSE composition (equivalent to primitive mantle [PM] and referred to as primitive upper mantle [PUM] by Becker et al., 2006), with workers utilizing a range of mantle rock types, including ultramafic massifs and ophiolites (e.g., Becker et al., 2006; Zhang et al., 2020), as well as using abyssal peridotites (e.g., Becker et al., 2006; Day et al., 2017a). These approaches for determining the absolute and relative abundances of the HSE in the bulk silicate Earth, and the extent of heterogeneity have drawbacks. For example, utilizing massif compositions requires effective subtraction of the effects of sometimes complex melt refertilization processes (e.g., Marchesi et al., 2014; Becker and Dale, 2016; Lorand and Luguet, 2016). Abyssal peridotites represent residues of ancient and modern depletion events (2% to >16%), which occurred > 0.5 Ga ago for some samples (e.g., Brandon et al., 2000; Harvey et al., 2006; Liu et al., 2008; Lassiter et al., 2014; Day et al., 2017a). Complications with these samples are that melt refertilization (e.g., Niu, 2004; Warren, 2016; Reisberg, 2021) and serpentinization or secondary alteration (e.g., Snow and Dick, 1995; Snow and Reisberg, 1995; Malvoisin, 2015) processes can affect their compositions. Furthermore, abyssal peridotites are difficult to sample, being either dredged or drilled typically from deep water locations (>3 km) and relatively rare exposures on the ocean floor, such that global coverage has hitherto not been obtained.

Currently, HSE and Os isotope data for abyssal peridotites are mainly from ultraslow to slow spreading ridges (e.g., Gakkel Ridge, Southwest Indian Ridge, Central Indian Ridge, Mid-Atlantic Ridge; Martin, 1991; Roy-Barman & Allègre, 1994; Snow & Reisberg, 1995; Snow & Schmidt 1998; Brandon et al., 2000; Luguet et al., 2001; 2003; Standish et al, 2002; Alard et al., 2005; Harvey et al., 2006; Sichel et al., 2008; Liu et al., 2008; 2009; Lassiter et al., 2014; Day et

al., 2017a). More limited data are available on the HSE abundances and Os isotopic composition of mantle beneath intermediate and fast spreading centers (Roy-Barman and Allègre, 1994; Snow and Schmidt, 1998; Rehkämper et al., 1999). Here we report new bulk rock $^{187}Os/^{188}Os$ and HSE abundance data for abyssal peridotites from the Pacific Ocean (Hess Deep along the East Pacific Rise (EPR) and from the Udintsev Fracture Zone (UFZ) along the Pacific Antarctic Ridge (PAR)). We compare these data with those obtained for abyssal peridotites from ultraslow to slow spreading ridges (e.g., Gakkel Ridge, Southwest Indian Ridge (SWIR), Central Indian Ridge (CIR), Mid-Atlantic Ridge (MAR)). Additionally, new bulk rock major and trace element abundances and mineral chemistry are reported for some samples to examine the relationship to spreading rate and melt depletion in abyssal peridotites, and to assess heterogeneity of mantle composition in terms of HSE abundances and Os isotope ratios and the implications this might have for mantle geodynamics.

2. SAMPLES AND METHODS

2.1 Samples

Dredged abyssal peridotites were analyzed from the fast-spreading East Pacific Rise (EPR), at Hess Deep (denoted AII) from cruise 125, leg 6, aboard the RV Atlantis II in May 1990. Dredged abyssal peridotites were also analyzed from the Pacific Antarctic Ridge (PAR), along two different locations of the Udintsev ridge, denoted as WEST03-MV12 and WEST03-MV13, from the WESTWARD (WEST03MV) cruise aboard the RV Melville in February 1994. Details for this cruise are reported in Castillo et al. (1998) and Niu (2004). New data are also reported for abyssal peridotites from slower spreading rates (Mid Atlantic Ridge, Central Indian Ridge and Southwest Indian Ridge) from the 1968 CIRCE cruise (Circe97) aboard the RV Argo, the 1970 ANTIPODE

149 cruise (ANTP) aboard the RV Melville, 1984 Protea Cruise (Prot05) aboard the RV Melville, the
150 1990 PLUME cruise (PLUM05) aboard the RV Thomas Washington, and the 2007 KNOX11RR
151 cruise aboard the RV Roger Revelle. Sample locations are reported in Figure 1 and Table 1.
152
153 ***2.2 Mineral compositions***
154 Major- and minor-element mineral compositions were obtained from polished mounts
155 containing olivine, pyroxene and spinel, and as polished thick sections for Hess Deep and PAR
156 samples, using a JEOL JXA-8230 electron probe micro analyzer (EPMA) at the University of
157 Colorado, USA (Department of Geological Sciences). Analyses were made with an accelerating
158 potential of 15 keV and a beam size of 5 μm. Beam currents were 30 nA for olivine and pyroxene
159 and 20 nA for spinel. Both natural and synthetic standards were used to calibrate the EMP and
160 were measured throughout analytical sessions to ensure data quality. Background and peak
161 counting times used were 20-30 s and standard PAP correction procedures were used. Detection
162 limits were ≤ 0.02 wt.% for Si, Al, Mg, Ca, Na, K and P and < 0.04 wt.% for Fe, Ti, Mn, V, Ni
163 and Cr.
164
165 ***2.3 Bulk rock major and trace element abundance analyses***
166 Major element compositions were measured by X-ray fluorescence (XRF) at Franklin and
167 Marshall College using a PW 2404 PANalytical XRF vacuum spectrometer following the protocol
168 described in Day et al. (2017a) and references therein. Repeated measurements of basaltic
169 reference material BHVO-2 allow estimations of precision and accuracy, with long-term
170 reproducibility of 0.1% for SiO_2, Al_2O_3, Fe_2O_{3T}, MgO and CaO, 0.2% for TiO_2, MnO and Na_2O,
171 and 0.3% for P_2O_5 (Table S1).

172

173 Trace elements analyses were performed on 100 mg of homogenized bulk rock powder
174 using a *Thermo Scientific* iCAP Qc ICP-MS at the Scripps Isotope Geochemistry Laboratory
175 (SIGL, University of California San Diego), following the method outlined in Day et al. (2014).
176 Samples were analyzed with several replicates of powdered peridotites HARZ-01 and PLUM05-
177 49, as well as BHVO-2, BCR-2 and BIR-1a, basaltic reference materials, used as standards to
178 confirm accuracy, with reproducibility on most of trace element abundances better than 10%
179 (Table S2).

180

181 ***2.4 Highly siderophile elements and Os isotopic compositions***

182 Osmium isotope and HSE abundance analyses were performed at the SIGL on ~900 mg of
183 homogenized powder from a larger powder aliquot. The samples were precisely weighed and
184 digested in sealed 20 cm borosilicate Carius tubes using a mixture of multiply Teflon distilled 12M
185 HCl (4 mL) and "purged" 15.7M HNO_3 (7 mL; expunged of Os using H_2O_2), with isotopically
186 enriched multi-element spikes (^{99}Ru, ^{106}Pd, ^{185}Re, ^{190}Os, ^{191}Ir, ^{194}Pt). Digestions lasted 72h hours
187 in an oven at a maximum temperature of 250°C. Osmium was purified by extracting CCl_4 three
188 times from the HCl/HNO_3, spike and sample mixture and then back extracting the Os from the
189 CCl_4 using HBr (Cohen and Waters, 1996), with further purification by micro-distillation (Birck
190 et al., 1997). The other HSE (Re, Pd, Pt, Ru, Ir) were recovered and purified from the residual
191 solutions using anion exchange column chemistry (e.g., Day et al., 2016b).

192

193 Acquisition of Os isotopic compositions were performed on a *Thermo Scientific* Triton
194 thermal ionization mass spectrometer in negative ion mode, with HSE abundances calculated from

isotopic ratios of Ir, Ru, Pt, Pd and Re measured using a *Thermo Scientific* iCaP Qc ICP-MS coupled to a *Cetac Aridus II* desolvating nebulizer. Osmium data were appropriately oxide-, fractionation-, spike- and blank corrected. Precision for $^{187}Os/^{188}Os$, determined by repeated measurements of 35 to 70 pg loads of the UMCP Johnson-Matthey standard, was better than ±0.2 % (2SD; 0.11382 ±0.00012; n = 10). These standard load sizes were smaller than unknown samples, which had >1 ng Os, and that typically ran with signal sizes of 200 K Cps on the largest mass isotope, with stable signals similar to the standards. Rhenium, Pd, Pt, Ir and Ru isotopic ratios were corrected for mass fractionation using the deviation of the standard average run on the day over the natural ratio of the element. External reproducibility on HSE analyses was better than 0.5% for 5 ppb solutions and all reported values are blank corrected. Peridotite standard reference materials (MUH-1, HARZ-01) run during the period of the analytical campaign in the SIGL are reported in Day et al. (2016a) and Snortum & Day (2020) and show good reproducibility and accuracy compared with literature data (e.g., Meisel & Horan, 2016). The total procedural blanks (n = 4) run with the samples had $^{187}Os/^{188}Os$= 0.209 ±0.090, with quantities (in pg) of 0.8 [Re], 7 [Pd], 22 [Pt], 15 [Ru], 3 [Ir] and 0.8 [Os]. These blanks resulted in negligible corrections to samples (<1% in most cases, Table S3).

3 RESULTS

3.1 Sample descriptions and mineral chemistry

Spinel grains in the PAR abyssal peridotites from WEST03MV-12 and WEST03MV-13 span a Mg# range of 58.4 to 70.6 and 68.7 to 72.7, and a Cr# range of 28.7 to 49.6 and 19.1 to 24.9, respectively, similar to plagioclase-free peridotites (e.g., SWIR peridotites, Seyler et al., 2003; global abyssal peridotite database, Warren, 2016). Spinel grains in Hess Deep (EPR) samples have

Mg# between 45.6 and 60.0, and Cr# between 47.3 and 52.0 (e.g., comparable to plagioclase-lherzolites from the SWIR; Paquet et al., 2016) (Figure S1a).

Forsterite contents in olivine grains range between 89.7 and 90.7, and between 90.0 and 90.6 in WEST03MV-12 and WEST03MV-13 samples, respectively (Table S4). Orthopyroxenes and clinopyroxenes in PAR samples have similar compositions: between $Wo_{0.01-0.07}En_{0.84-0.89}Fs_{0.08-0.10}$ and $Wo_{0.32-0.49}En_{0.47-0.62}Fs_{0.05-0.07}$ for WEST03MV-12 peridotites, and between $Wo_{0.01-0.11}En_{0.81-0.89}Fs_{0.09-0.10}$ and $Wo_{0.35-0.49}En_{0.46-0.59}Fs_{0.04-0.06}$ for the WEST03MV-13 peridotites (Figure S1b). WEST03MV-12 and WEST03MV-13 peridotites have Cr_2O_3 contents that range from 0.66 to 1.08 wt.% and from 0.43 to 0.96 wt.% in orthopyroxenes, and from 0.95 to 1.43 wt.% and from 0.56 to 1.32 wt.% in clinopyroxenes, respectively (Table S4). These values are within the compositions of abyssal peridotites from the global ridge system (e.g., Warren, 2016). Olivine, orthopyroxene and clinopyroxene grains in the EPR samples were not fresh enough to conduct analyses on.

3.2 Bulk rock major and trace element abundances

Hess Deep abyssal peridotites tend to have lower anhydrous-corrected Al_2O_3, TiO_2 and CaO, and higher MgO contents than to those from the Pacific Antarctic Ridge (Figure 2, Table S5). The WEST03MV-13 peridotites generally have lower Al_2O_3, TiO_2 and CaO (and Fe_2O_{3T} to a lesser extent) at a given MgO than the WEST03MV-12 peridotites suggesting heterogeneity at the scale of the fracture zone that they were dredged from. All these peridotites show a positive correlation between Al_2O_3 and CaO, with Hess Deep peridotites being both tightly grouped in terms of composition and having the most refractory (lowest) Al_2O_3 and CaO contents. Overall, the Pacific abyssal peridotites overlap the trend defined by abyssal peridotites from ridges with

241 slower spreading rates (Day et al., 2017a).

242

243 Abyssal peridotites from the UFZ along the PAR are characterized by having subchondritic
244 rare earth element (REE) abundances, and show pronounced LREE-depleted patterns, which are
245 similar to abyssal peridotites from the Mid-Atlantic Ridge, and some samples from the SWIR and
246 Gakkel ridge (Day et al., 2017a) (Figures 3, S2 and Table S6). Samples from the West region span
247 a larger range of REE abundances. Abyssal peridotites from Hess Deep are depleted in the heavy
248 REE, with REE patterns slightly depleted in the light REE (LREE) relative to the HREE, and
249 strong positive anomalies for Eu, suggesting melt impregnation and plagioclase crystallization. A
250 few samples from the PAR, SWIR and CIR also show negative Ce anomalies. Overall, abyssal
251 peridotites from the WEST03MV-13 dredge tend to have higher Nb and Ta abundances, and lower
252 Zr and Hf abundances than those from the WEST03MV-12 dredge. Abyssal peridotites from Hess
253 Deep exhibit depleted patterns in Rb, Ba, Nb, Ta, Zr and Hf compared to other Pacific peridotites.
254 Overall, incompatible trace element (ITE) and REE abundances for abyssal peridotites from the
255 SWIR are in good agreement with data reported in previous studies (e.g., Day et al, 2017a) (Figures
256 3, S2 and Table S6).

257

258 Abyssal peridotites from the CIR reported in this study show more depleted patterns in the
259 REE, and for the ITE in general with lower Nb contents (and slightly higher Ta abundances), than
260 previously reported samples (e.g., Day et al., 2017a). PLUM05 abyssal peridotite samples from
261 the MAR have HREE similar to those from the same ocean basin in the literature but are more
262 enriched in the LREE and have more pronounced positive Eu anomalies. They also exhibit higher
263 contents in Rb, Ba, Nb and Ta, but lower Zr and Hf abundances than those from Day et al. (2017a).

264 Most abyssal peridotites show elevated concentrations in fluid mobile elements such as U and Sr
265 which are enriched in seawater (Figure S2).
266
267 ***3.3 Highly siderophile element abundances and Os isotopic compositions***
268 Bulk rock Re-Os isotope and highly siderophile-element (HSE: Re, Pd, Pt, Ru, Ir, Os)
269 abundance measurements for Pacific abyssal peridotites and some Southwest Indian Ridge and
270 Central Indian Ridge peridotites are reported in Table 1. PAR samples from the WEST03MV-13
271 dredge have BSE-like HSE patterns with variable rhenium depletion, whereas samples from the
272 WEST03MV-12 dredge have more variable Re, Pd and Pt abundances (Figure 4), similar to those
273 reported previously (Roy-Barman and Allègre, 1994; Snow and Schmidt, 1998; Rehkämper et al.,
274 1999). Two of the Hess Deep samples have patterns that are akin to BSE, while the other samples
275 show variable degrees of rhenium depletion relative to BSE. WEST03MV-12 and WEST03MV-
276 13 abyssal peridotites have average Pd/Ir ratios of 1.4 ± 0.6 and 1.4 ± 1.1 (2 SD), and average
277 Ru/Ir ratios of 1.7 ± 0.2 and 1.8 ± 0.4 respectively (Figure 5). Hess Deep samples show average
278 ratios slightly higher but within uncertainties at 1.9 ± 1.1 and 2.0 ± 0.6 for Pd/Ir and Ru/Ir ratios,
279 respectively. Moreover, HSE patterns for the Pacific abyssal peridotites are like those from the
280 Mid-Atlantic Ridge, and some of the abyssal peridotites from the Southwest Indian Ridge (Day et
281 al., 2017a and references therein).
282
283 Pacific Antarctic Ridge peridotites show similar ranges and averages in $^{187}Os/^{188}Os$
284 (WEST03MV-12: 0.1264 ± 0.0054; WEST03MV-13: 0.1272 ± 0.0082; all uncertainties are 2 SD),
285 and are slightly more radiogenic, on average, than the samples from Hess Deep (0.1247 ± 0.0030)
286 (Figure 6), with an average value of 0.1264 ± 0.0063 for all Pacific abyssal peridotites from this

study. Using the Os abundances in the samples to calculate a weighted mean, we obtained a $^{187}Os/^{188}Os$ ratio of 0.1263. These new data overlap the trend defined by abyssal peridotites from slower spreading ridges (Snow & Schmidt, 1998; Rehkämper et al., 1999; Luguet et al., 2001; Liu et al., 2009; Lassiter et al., 2014; Day et al., 2017a), but are generally more radiogenic than mantle peridotites obtained from Pacific Ocean Islands (Snortum et al., 2019), which offer an alternate view of the Pacific oceanic mantle lithosphere.

4 DISCUSSION

4.1 Alteration and melt infiltration

Most abyssal peridotites have experienced serpentinization (<400 °C) and/or sea-floor weathering (~0°C) under both oxidizing and reducing conditions (e.g., Snow & Dick, 1995; Bach et al., 2004; Paulick et al., 2006; Klein et al., 2013; Malvoisin, 2015). Samples in this study exhibit evidence for secondary alteration, manifested as loss on ignition (LOI) values of between ~5 and 17%, reflecting the presence of serpentine and other alteration minerals. As noted for abyssal peridotites from a range of spreading ridge environments (Niu, 2004; Harvey et al., 2006; Day et al., 2017a), elevated concentrations of fluid mobile elements, occur in many of the samples, consistent with modification by interaction with seawater (e.g., U, Sr, K, P, Na, LREE; e.g., Frisby et al., 2016). However, most major and trace elements appear unaffected by alteration processes. Prior work has suggested that $^{187}Os/^{188}Os$ (e.g., Snow & Reisberg, 1995; Standish et al., 2002), Re and Pd (e.g., Luguet et al., 2003; Harvey et al., 2006) can be modified by serpentinization and seafloor alteration processes but that, in general, abyssal peridotite HSE abundances are typically not strongly affected by such processes (e.g., Liu et al., 2009; Day et al., 2017a). In agreement with those studies, we find no correlation with LOI and HSE contents and Os isotopic

310 compositions (Figure S3). Indeed, it has been shown that even strongly steatized serpentinite rocks
311 faithfully preserve original HSE abundances (Day et al., 2017b). Overall, we conclude that the
312 bulk rock abyssal peridotite HSE compositions predominantly reflect their high temperature
313 mantle petrogenesis.
314
315 Melt refertilization in abyssal peridotites (Niu, 2004; Seyler et al., 2004; Warren et al.,
316 2009; Warren, 2016) can also lead to precipitation of metasomatic sulphides rich in Pd and the
317 other HSE (Alard et al., 2000; Luguet et al., 2003). Evidence for melt refertilization in the sample
318 suite is provided by the enrichments of non-fluid mobile highly incompatible elements in all
319 samples (Figure 3). Enrichments of two or three orders of magnitude in the high field strength
320 elements (HFSE: Nb, Ta, Ti, Zr, Hf) relative to what would be expected for partial melting residues
321 are strong indicators of melt refertilization in Pacific abyssal peridotites (Figure 3), along with
322 some LREE-enriched peridotites, as observed in slower-spreading ridges (Niu et al., 2004; Warren,
323 2016; Day et al., 2017a). This melt infiltration has been variable between the sample suites, with
324 plagioclase-rich melt infiltration possible in some sample suites (e.g., Hess Deep). These
325 observations match with hand-specimen observations for AII125-6-4D-18, which include minor
326 melt infiltration veins that are cross-cut by serpentine. Moreover, spinel grains in the Pacific
327 abyssal peridotites plot within the lower part of the abyssal peridotite field, with relatively low Cr#
328 at a given Mg#, which is often associated with the presence of pyroxenite-veins in the samples
329 (e.g., Warren, 2016).
330
331 Melt infiltration events appear to have limited impact on Pt, Ru, Ir or Os abundances or Os
332 isotopes in Pacific abyssal peridotites. In contrast, samples display variable Re contents, and Pd

333 contents to a lesser extent (Figure 4), which may be attributed to various degrees of refertilization
334 by melts. As shown previously, basaltic melts typically have more radiogenic $^{187}Os/^{188}Os$, but
335 substantially lower Os contents than peridotites, meaning that only high degrees of melt-rock
336 reaction will lead to modification of peridotite HSE compositions (Day et al., 2017a). The
337 generally high Os contents of the samples (~2-9 ppb) means that melt refertilization would only
338 be notable at melt-rock ratios in excess of ten, which is not consistent with immobile incompatible
339 trace element addition in all samples and suggests melt-rock ratios less than one. Even the
340 peridotite with the lowest Os content in the sample set (CIRCE97-HD-2; 0.19 ppb Os) has
341 $^{187}Os/^{188}Os$ within the range of the other peridotites, and distinct from more radiogenic MORB
342 melts (e.g., Gannoun et al., 2016). These lines of evidence suggest that sulfide melt addition is not
343 a significant driver in Pt, Ru, Ir or Os abundances or $^{187}Os/^{188}Os$ in the studied abyssal peridotites.
344 Conversely, melt refertilization can be pervasive and variable in extent from ultraslow to fast
345 spreading ridges in modifying Re and Pd abundances (up to a factor 10 for Re abundances; Figure
346 4).
347
348 ***4.2 Recent versus ancient processes acting on abyssal peridotites***
349 Melt depletion processes can fundamentally modify peridotite compositions (e.g., Becker et
350 al., 2006; Reisberg, 2021). It is possible to estimate the degree of melt depletion experienced by
351 peridotites using a range of methods. For example, non-modal fractional melting models can be
352 used to estimate melt depletion in abyssal peridotites based on REE abundances (here using model
353 parameters outlined in Day et al., 2017a). An increase in melt depletion is associated with lower
354 absolute REE abundances and higher depletion in the LREE relative to the HREE. The REE
355 modeling calculations suggest 3-20% melt extraction for the WEST03MV-12 peridotites, 8-13%

for the WEST03MV-13 peridotites, and 15-20% for the EPR peridotites. These estimates are consistent to slightly higher than calculations of melt depletion using Cr# in spinel grains from the same samples (e.g., Batanova et al., 1998; Hellebrand et al., 2001): 13.7-19.0%, 9.6-12.3% and 18.4-19.5% respectively (Table S4). The more BSE-like HSE patterns in the WEST03MV-13 peridotites relate to more limited melt depletions than in other abyssal peridotite samples from the PAR and Hess Deep. The estimated high degrees of melt loss in some of the peridotites (WEST03MV-12 and Hess Deep) are consistent with clinopyroxene being nearly consumed within the mineral assemblage (Ol + Opx + Cpx + Sp) during partial melting. Correspondingly, melt extraction at fast-spreading ridges ranges up to higher values than those calculated for slow and ultraslow-spreading ridges (e.g., Warren, 2016; Day et al., 2017a) (Figure S4).

Melt extraction in the mantle typically leads to the formation of residual peridotites depleted in Re, Pd ± Pt, relative to Ru, Ir and Os, reflecting the extraction of sulfide melt along with silicate melt, or dissolution of sulfides into the melt and formation of refractory platinum group minerals (e.g., Alard et al., 2000; Luguet et al., 2003; Ballhaus et al., 2006; Liu et al., 2009; Reisberg, 2021). Notably, Pacific abyssal peridotites tend to have BSE-like to fractionated HSE patterns with relative depletion in Re, Pd and Pt: all Pacific abyssal peridotites show similar ranges for $(Pd/Ir)_n$ and $(Pt/Ir)_n$ (WEST03MV-12 dredge: 0.5- 1.2 and 0.6 – 0.9; WEST03MV-13 dredge: 0.5-1.6 and 0.5-1.0; EPR: 0.9-1.8 and 0.6-1.6 respectively). Pacific Antarctic Ridge samples with low degrees of melt depletion (WEST03MV-13) have BSE-like HSE patterns with variable rhenium depletion, whereas samples with higher degrees of melt depletion (WEST03MV-12) have more variable Re, Pd and Pt abundances (Figure 4). Two of the Hess Deep samples have patterns that are akin to BSE, while the other samples show different degrees of rhenium depletion, suggesting that, in all

379 cases, melt depletion has modified the original HSE abundances. The average total HSE content
380 decreases with decreasing melt depletion degree (Figure S5), suggesting that the variability
381 observed between the different ocean basins in term of HSE abundances can be explained by
382 petrogenetic processes.
383
384 Melt depletion in peridotites decreases the incompatible element abundances. Positive
385 correlations exist between Al_2O_3, as well as the HREE and Y, and $^{187}Os/^{188}Os$ for the Pacific
386 abyssal peridotites (Figure 6), as observed for peridotites from slower spreading ridges (e.g.,
387 Reisberg and Lorand, 1995; Parkinson et al., 1998; Lassiter et al., 2014; Day et al., 2017a). Positive
388 relationships also exist between Al_2O_3 and Re/Ir and Pd/Ir, but do not occur for Pt/Ir, Ru/Ir or
389 Os/Ir, which are essentially invariant with decreasing Al_2O_3 (Table 1). Rhenium and Pd
390 abundances in abyssal peridotites are depleted during melt loss, whereas Pt, Ru, Ir and Os
391 abundances and $^{187}Os/^{188}Os$ are less affected by such processes. Consequently, these correlations
392 reflect variable melt loss in the peridotite suite. The, correlation between $^{187}Os/^{188}Os$ and Al_2O_3
393 contents in bulk rock abyssal peridotites further implies that some of this melt depletion is also
394 ancient, as $^{187}Os/^{188}Os$ in these rocks tracks long-term melt depletion, where rocks with low Al_2O_3
395 also have low $^{187}Re/^{188}Os$. Pre-existing heterogeneities in peridotites have been noted in previous
396 ^{187}Re-^{187}Os studies, reporting Re depletion ages (T_{RD} = 1/1.67 × 10-11 × ln{[(0.127 –
397 $^{187}Os/^{188}Os_{sample}$)/0.40186]+1}; where T_{RD} ages represent minimum depletion ages, assuming no
398 ingrowth from ^{187}Re in abyssal peridotites since melt depletion) as ancient as 2 Ga for abyssal
399 peridotites (e.g., Harvey et al., 2006; Liu et al., 2008; Lassiter et al., 2014; Day et al., 2017a), as
400 well as for ophiolite peridotites (e.g., Büchl et al., 2004; Schulte et al., 2009; O'Driscoll et al.,
401 2012, 2015) and mantle peridotites from ocean islands (Snortum et al., 2019). In this respect, it is

notable that the concept of the T_{RD} model age was originally developed for highly refractory cratonic peridotites, where the estimated degree of melt extraction is ~30 to 50%, leading to nearly Re-free peridotitic residues (Walker et al., 1989; Luguet and Pearson, 2019; Reisberg, 2021, and references therein). Nonetheless, measured $^{187}Os/^{188}Os$ below the BSE or even chondritic values in mantle peridotites must reflect long-term rhenium depletion.

Rhenium depletion ages for Pacific abyssal peridotites range up to 1.3 Ga for peridotites from the WEST03MV-12 dredge, up to 1.5 Ga for those from the WEST03MV-13 dredge, and up to 0.9 Ga for Hess Deep (Figure 5). The oldest rhenium depletion ages are therefore in the samples with the lowest degrees of melt depletion. The average Re depletion ages are 0.5 ± 0.3 Ga, 0.6 ± 0.5 Ga and 0.7 ± 0.2 Ga respectively, which are similar to previous estimates from abyssal peridotites (Lassiter et al., 2014; Day et al., 2017a). The distinction between ancient melt depletion and recent melt depletion at the ridge remains one of the most challenging issues to deconvolve in abyssal peridotites. No correlations between $^{187}Os/^{188}Os$ or T_{RD} ages with degree of partial melting (or melt depletion, F) are observed, suggesting that separating pre-existing melt depletion from recent-ridge melt depletion cannot be directly established. Nevertheless, Pacific abyssal peridotites with low Pd/Ir also show ancient T_{RD} ages, similar to samples from slower spreading ridges (e.g., Lassiter et al., 2014; Day et al., 2017a), indicating that abyssal peridotites preserve significant pre-existing melt depletion, up to or exceeding 2 Ga, in some cases (Figure 5).

4.3 Pacific Ocean mantle composition

Collectively, Pacific abyssal peridotites have similar distributions and variations in the abundances of the HSE, as well as slightly more radiogenic $^{187}Os/^{188}Os$, relative to Pacific mantle

425 xenoliths (Figure 6a) (Bizimis et al., 2007; Jackson et al., 2016; Snortum et al., 2019). Mantle
426 xenoliths preserve melt depletion ages up to 1.5 Ga in Aitutaki (Cook Islands: Snortum et al.,
427 2019), 1.5 Ga in Savai'i, 1.8 Ga in Tubuai (Samoa and Austral Islands respectively: Jackson et al.,
428 2016) and as ancient as 2 Ga in O'ahu (Hawaii: Bizimis et al., 2007), similar to T_{RD} ages reported
429 for Pacific abyssal peridotites. These observations indicate that the Pacific oceanic mantle records
430 heterogeneous melt-depletion from both ancient and more recent melt depletion events. These melt
431 depletion events can be up to 2 Ga and, in this sense, are similar to observations from global
432 oceanic lithosphere (e.g., Brandon et al., 2000; Harvey et al., 2006; Liu et al., 2008, 2009; Lassiter
433 et al., 2014; Day et al., 2017a). Even though Pacific abyssal peridotites and mantle xenoliths only
434 provide a glimpse of the Pacific oceanic plate, often at the hand-sample scale, they show evidence
435 for significant heterogeneities at short length scales due to prior melt depletion events up to 2 Ga
436 ago, as well as strong similarities in average HSE abundances and Os isotope compositions to
437 abyssal peridotites from the Atlantic, Indian or Arctic Ocean basins.
438
439 ***4.4 Composition of the Bulk Silicate Earth deduced from abyssal peridotites***
440 Average HSE abundances and Os isotope compositions for measured abyssal peridotites from
441 the global mid-ocean ridge system show no correlation with spreading rate (Figure 7 and S6). This
442 observation is important because different melting processes at slow and ultraslow spreading
443 ridges versus fast spreading ridges could conceivably yield differences in modern melt depletion
444 recorded in abyssal peridotites, but this is not the case. The $^{187}Os/^{188}Os$ composition of the BSE
445 recalculated with the new Pacific abyssal peridotites is 0.1265 ± 0.0031 (n = 230), and 0.1250 ±
446 0.0040 for peridotites with > 2 ppb Os. These values are close to those reported by Lassiter et al.
447 (2014) for the convecting upper mantle and by Day et al. (2017a) for the depleted MORB mantle

448 (0.1245 and 0.1247 ± 0.0075 respectively). Following a similar approach as Day et al. (2017a), we
449 recalculate the average composition of the BSE using abyssal peridotites with Al_2O_3 content > 2
450 wt.% from all mid-ocean ridge systems (Figure 8). We obtain 0.34 ± 0.38 (1 s.d.) ppb [Re], 4.87
451 ± 2.67 ppb [Pd], 7.29 ± 1.88 ppb [Pt], 7.40 ± 1.89 ppb [Ru], 3.84 ± 1.12 ppb [Ir] and 3.36 ± 1.09
452 ppb [Os] (Figure 8). Estimates for the Arctic and Indian Oceans give comparable values to those
453 of the global ridge system estimate (Figure 8). Note that the Atlantic Ocean estimate appears
454 slightly depleted, and the Pacific Ocean is slightly enriched in the HSE, compared with the global
455 BSE estimate (Figure 8). These differences can be attributed to variable degrees of ancient and
456 modern partial melting affecting the peridotites. Similar results are obtained when the data are
457 regressed to a BSE Al_2O_3 value of 4 to 4.5 wt.% (see Day et al., 2017a).
458
459 The reevaluated composition for the BSE, including the new Pacific abyssal peridotite data,
460 does not significantly change the average estimates for the BSE previously reported for abyssal
461 and oceanic peridotites (Becker et al., 2006; Chatterjee and Lassiter, 2016; Day et al., 2017a), or
462 for continental peridotites (Becker et al., 2006; Chatterjee and Lassiter, 2016). Our results for
463 Pacific abyssal peridotites confirm that the BSE estimated from abyssal peridotites does not show
464 high Pd/Ir and Pd enrichment as reported by Becker et al. (2006), and Chatterjee and Lassiter
465 (2016). This discrepancy between the two estimates of the BSE compositions is thought to result
466 from Pd enrichment in the continental-derived peridotites used for the calculation due to melt-
467 refertilization (e.g., Aulbach et al., 2016; Luguet and Reisberg, 2016; Becker and Dale, 2016).
468 Overall, these observations lead to the idea that the BSE shows an abundance range for the most
469 incompatible HSE (Re, Pd) that can exceed one hundred percent, but that more compatible HSE
470 (Pt, Ru, Ir, Os) show less than 30% abundance variation. These variations can be accounted for by

melting processes acting on abyssal peridotites over <2 Ga.

4.5 Implications of a relatively homogeneous convecting mantle for the HSE

Abyssal peridotites from fast to intermediate spreading ridges reveal few, if any, systematic differences in the distribution and behavior of the HSE, compared with slow to ultraslow spreading ridges, despite generally higher degrees of melt depletion (Figures 7 and 8). Additionally, estimates of the $^{187}Os/^{188}Os$ isotope composition of the BSE based on abyssal peridotites show little to no difference to oceanic mantle xenoliths (e.g., Chatterjee and Lassiter, 2016; Snortum et al., 2019) and samples from peridotite massifs (e.g., Becker et al., 2006). Taking the available global abyssal peridotite sample set and using Al_2O_3 > 2 wt.%, HSE and Os isotope compositions argue in favor of present-day convecting mantle composition, with Pt, Ru, Ir and Os abundance variations at <±30% and $^{187}Os/^{188}Os$ variations at ~6% (2SD) for the global abyssal peridotite dataset. As noted previously, this variation can be accounted for by recent rather than ancient (>2 Ga) processes.

Compared with abyssal peridotites (e.g., Day et al., 2017a and this study), Archean mantle peridotites from West Greenland (3.8 Ga) and Western Australia (3.46 Ga) have similar broadly chondritic $^{187}Os/^{188}Os$ compositions and Os concentrations, arguing in favor of the HSE being added to the Earth, transported and homogenized within the mantle by ~3.8 Ga (Bennett et al., 2002; van de Löcht et al., 2018). Homogeneous Ru isotope compositions have been reported in Archean ultramafic rocks younger than 3.5 Ga (Pilbara Craton, Australia: 3.5 - 3.2 Ga; Abitibi greenstone belt, Canada: 2.7 Ga; Bushveld, South Africa: 2.05 Ga), as well as in Phanerozoic oceanic and continental mantle domains, and are undistinguishable from the modern terrestrial

494 mantle (Bermingham and Walker, 2017; Fischer-Gödde et al., 2020). These lines of evidence all
495 support a relatively homogenized BSE in terms of HSE abundances and Os isotope ratios since at
496 least the Archaean, where variations reflect melting processes within the mantle, rather than
497 heterogeneities incorporated during Earth's accretion.
498
499 Based on HSE abundances, it has been proposed that ~0.5 to 0.8% of Earth's present mass
500 was accreted after core formation, if all HSE delivered by these impacts were retained in the
501 mantle, rather than being lost to the core or through inefficient impact retention (Becker et al.,
502 2006; Day et al., 2016a). Consequently, late accretion impacts might have been expected to leave
503 graininess in HSE abundances in Earth's mantle. This is because some moderate to large size
504 impactors may not have been capable of completely remelting Earth's mantle. From a geological
505 perspective, Eoarchean ultramafic rocks from Greenland (3.8 - 3.7 Ga), and Mesoarchean
506 chromitites from Seqi, Greenland (minimum age of 3 Ga) exhibit ^{100}Ru excess (Fischer-Gödde et
507 al., 2020), arguing in favor of a heterogeneous delivery of the HSE to the Earth during late
508 accretion. Similarly, evidence for grainy accretion has been suggested for other bodies, such as
509 Vesta (Day et al., 2012). Numerical impact models also support that delivery of silicate and metal
510 to the Earth by large planetesimals was heterogeneous, leading to projectile material being
511 concentrated within localized domains of Earth's mantle and producing isotopic anomalies in W,
512 Mo and Ru isotopes (Marchi et al., 2018; Maas et al., 2021).
513
514 Geochemical arguments in favor of heterogeneities imparted to the mantle during accretion
515 include positive μ^{182}W preserved in most Eoarchean rocks studied to date, which have been
516 interpreted to indicate that late accreted materials were not evenly distributed in Earth's mantle,

and not well mixed in the BSE (Willbold et al., 2011). Such heterogeneities are not evident in the convecting mantle, with basalts from mid-ocean ridges and ocean islands measured to date lacking positive $\mu^{182}W$ anomalies (e.g., Mundl et al., 2017). The HSE have also been argued to have been heterogeneously distributed within the early mantle from observations that Archean (3.5 – 3.2 Ga) komatiites from the Barberton greenstone belt (South Africa) and the Pilbara craton (Western Australia) apparently record depleted HSE compositions for their mantle sources relative to late Archean and younger komatiites (Maier et al., 2009). Arguments in favor of HSE heterogeneities imparted to the mantle by late accretion are not without controversy, however, where it has been argued that komatiites are not faithful recorders of mantle source compositions (Waterton et al., 2021).

Because the HSE appear to be homogeneously mixed in the present-day convecting mantle, we favor that whatever HSE input was accreted to the Earth, these heterogeneities have been relatively efficiently mixed into the mantle through convective processes. Anomalies in the HSE, including Ru, as well as Mo and W in Archean crustal rocks can be interpreted to reflect late accretion heterogeneity within the Earth that is well-recorded within isolated crustal and lithospheric fragments. For example, the mantle beneath southwest Greenland had not yet fully equilibrated with late accretion material by 3.7 Ga ago (Fischer-Gödde et al., 2020). This is consistent with the average mantle homogenization timescale of ~1.2 Ga calculated from the combined $^{186}Os/^{188}Os$-$^{187}Os/^{188}Os$ isotopic and Pt/Os and Re/Os variability in peridotites (e.g., Chatterjee and Lassiter, 2016). Other isotopic systems, such as the short lived ^{146}Sm-^{142}Nd system, lead to younger mantle homogenization timescales (~0.4 Ga) as well as a fast mantle stirring rate (e.g., Chatterjee and Lassiter, 2016; Hyung and Jacobsen, 2020).

In contrast with lithophile incompatible elements, which are sensitive to resetting by melt refertilization in peridotites, the Re-Os and Pt-Os isotope systems are less susceptible to similar petrogenetic processes. As such, the mixing timescale inferred from Os isotopes in abyssal peridotites of around 0.5-0.7 Ga is approximately consistent with timescales predicted for the whole mantle convection. Hoffman and McKenzie (1985) showed that any convecting region of the upper mantle will be well mixed on a horizontal scale of at least 2000 km in 400 Ma, or 8500 km in 1.5 Ga, suggesting that large scale heterogeneities would be destroyed within Earth's lifetime. Our data support this contention. Nonetheless, elemental and isotopic anomalies that are thought to reflect mantle heterogeneities have been recorded in ocean island basalts (e.g., HSE in the Réunion cumulate xenoliths, Peters et al., 2016; W isotope anomalies in modern flood basalts: Rizo et al., 2016; and modern ocean island basalts: Mundl et al., 2017; Mundl-Petermeier et al., 2019, 2020; Peters et al., 2021). These suggest that distinct mantle domains might have been effectively isolated and preserved from the convecting upper mantle through most of the Earth's history (e.g., Allègre and Turcotte, 1985).

5 CONCLUSIONS

This global survey of abyssal peridotites from fast to intermediate spreading ridges reveals few if any systematic differences in the distribution and behavior of the HSE, compared with slow to ultraslow spreading ridges, despite variable degrees of melt depletion. Melt refertilization is pervasive and variable in extent from ultraslow to fast spreading ridges and can modify Re and Pd quite significantly. Across ocean basins and independently of spreading rates, the HSE appear relatively homogeneous in the BSE. Using abyssal peridotites with Al_2O_3 content > 2 wt.% from

563 all mid-ocean ridge systems, including the new Pacific abyssal peridotite data, we recalculated the
564 average composition of the BSE of 0.30 ± 0.33 ppb [Re], 4.94 ± 2.35 ppb [Pd], 7.13 ± 2.16 ppb
565 [Pt], 7.22 ± 3.71 ppb [Ru], 3.79 ± 1.84 ppb [Ir] and 3.77 ± 1.45 ppb [Os]. Variability observed
566 between the different ocean basins, if any, can most likely be explained by partial melting
567 processes. The variations in HSE abundances currently observed within the convecting mantle
568 sampled by abyssal peridotites are primarily due to partial melting and melt refertilization
569 processes over the past 2 Ga rather than to significant HSE heterogeneity of the post-Archean
570 mantle. Preservation of ancient melt depletion heterogeneities in some oceanic peridotites, with
571 osmium T_{RD} ages exceeding 1 Ga and highly depleted Hf isotope signatures measured in
572 clinopyroxene grains (Stracke et al., 2011; Sanfilippo et al., 2019) suggests some refractory
573 domains formed through ancient melt depletion can also be partially preserved in the convecting
574 upper mantle.
575

576 **ACKNOWLEDGMENTS**

577 This work was largely supported by a University of California San Diego Academic Senate Award,
578 and in part, by the NSF Petrology and Geochemistry program (NSF EAR 1447130 and EAR
579 1918322 to JMDD). We are grateful to Alex Hangsterfer (SIO Geological Collections) for
580 assistance with sample curation. Dean Poeppe and Garrett Stewart are thanked for assistance with
581 sample preparation. Constructive comments from David van Acken, the Associate Editor, Andreas
582 Stracke, and two anonymous reviewers are gratefully acknowledged.
583

584 **REFERENCES CITED**

585 Alard, O., Luguet, A., Pearson, N. J., Griffin, W. L., Lorand, J. P., Gannoun, A., ... & O'Reilly, S.
586 Y. (2005). In situ Os isotopes in abyssal peridotites bridge the isotopic gap between
587 MORBs and their source mantle. *Nature*, *436*(7053), 1005-1008.

588 Alard, O., Griffin, W. L., Lorand, J. P., Jackson, S. E., & O'Reilly, S. Y., 2000. Non-chondritic
589 distribution of the highly siderophile elements in mantle sulphides. *Nature*, *407*, 891-894.

590 Allègre, C. J., & Turcotte, D. L., 1985. Geodynamic mixing in the mesosphere boundary layer and
591 the origin of oceanic islands. *Geophysical Research Letters*, *12*(4), 207-210.

592 Aulbach, S., Mungall, J. E., & Pearson, D. G. (2016). Distribution and processing of highly
593 siderophile elements in cratonic mantle lithosphere. *Reviews in Mineralogy and*
594 *Geochemistry*, *81*(1), 239-304.

595 Bach, W., Garrido, C. J., Paulick, H., Harvey, J., & Rosner, M. (2004). Seawater-peridotite
596 interactions: First insights from ODP Leg 209, MAR 15°N. *Geochemistry, Geophysics,*
597 *Geosystems*, *5*(9).

598 Ballhaus, C., Bockrath, C., Wohlgemuth-Ueberwasser, C., Laurenz, V., & Berndt, J. (2006).
599 Fractionation of the noble metals by physical processes. *Contributions to Mineralogy and*
600 *Petrology*, *152*(6), 667-684.

601 Batanova, V. G., Suhr, G., & Sobolev, A. V. (1998). Origin of geochemical heterogeneity in the
602 mantle peridotites from the Bay of Islands ophiolite, Newfoundland, Canada: ion probe
603 study of clinopyroxenes. *Geochimica et Cosmochimica Acta*, *62*(5), 853-866.

604 Becker, H., & Dale, C. W. (2016). Re–Pt–Os isotopic and highly siderophile element behavior in
605 oceanic and continental mantle tectonites. *Reviews in Mineralogy and*
606 *Geochemistry*, *81*(1), 369-440.

607 Becker, H., Horan, M. F., Walker, R. J., Gao, S., Lorand, J. P., & Rudnick, R. L. (2006). Highly
608 siderophile element composition of the Earth's primitive upper mantle: constraints from
609 new data on peridotite massifs and xenoliths. *Geochimica et Cosmochimica Acta*, *70*(17),
610 4528-4550.

611 Bennett, V. C., Nutman, A. P., & Esat, T. M. (2002). Constraints on mantle evolution from
612 $^{187}Os/^{188}Os$ isotopic compositions of Archean ultramafic rocks from southern West
613 Greenland (3.8 Ga) and Western Australia (3.46 Ga). *Geochimica et Cosmochimica*
614 *Acta*, *66*(14), 2615-2630.

615 Birck, J. L., Barman, M. R., & Capmas, F. (1997). Re-Os isotopic measurements at the femtomole
616 level in natural samples. *Geostandards newsletter*, *21*(1), 19-27.

617 Bermingham, K. R., & Walker, R. J. (2017). The ruthenium isotopic composition of the oceanic
618 mantle. *Earth and planetary science letters*, *474*, 466-473.

619 Bizimis, M., Griselin, M., Lassiter, J. C., Salters, V. J., & Sen, G. (2007). Ancient recycled mantle
620 lithosphere in the Hawaiian plume: osmium–hafnium isotopic evidence from peridotite
621 mantle xenoliths. *Earth and Planetary Science Letters*, *257*(1-2), 259-273.

622 Bottke, W. F., Walker, R. J., Day, J. M., Nesvorny, D., & Elkins-Tanton, L. (2010). Stochastic late
623 accretion to Earth, the Moon, and Mars. *Science*, *330*(6010), 1527-1530.

624 Brandon, A.D., Snow, J.E., Walker, R.J., Morgan, J.W., Mock, T.D. (2000) ^{190}Pt-^{186}Os and ^{187}Re-
625 ^{187}Os systematics of abyssal peridotites. Earth and Planetary Science Letters, 177, 319-335.

626 Brenan, J. M., Bennett, N. R., & Zajacz, Z. (2016). Experimental results on fractionation of the
627 highly siderophile elements (HSE) at variable pressures and temperatures during planetary
628 and magmatic differentiation. *Reviews in Mineralogy and Geochemistry*, *81*(1), 1-87.

629 Brenan, J. M., & McDonough, W. F. (2009). Core formation and metal–silicate fractionation of
630 osmium and iridium from gold. *Nature Geoscience*, *2*(11), 798.

631 Büchl, A., Brügmann, G., & Batanova, V. G. (2004). Formation of podiform chromitite deposits:
632 implications from PGE abundances and Os isotopic compositions of chromites from the
633 Troodos complex, Cyprus. *Chemical Geology*, *208*(1-4), 217-232.

634 Castillo, P. R., Natland, J. H., Niu, Y., & Lonsdale, P. F. (1998). Sr, Nd and Pb isotopic variation
635 along the Pacific–Antarctic risecrest, 53–57 S: implications for the composition and
636 dynamics of the South Pacific upper mantle. *Earth and Planetary Science Letters*, *154*(1-
637 4), 109-125.

638 Chatterjee, R., & Lassiter, J. C. (2016). ^{186}Os/^{188}Os variations in upper mantle peridotites:
639 Constraints on the Pt/Os ratio of primitive upper mantle, and implications for late veneer
640 accretion and mantle mixing timescales. *Chemical Geology*, *442*, 11-22.

641 Chou, C. L. (1978). Fractionation of siderophile elements in the Earth's upper mantle. In *Lunar*
642 *and Planetary Science Conference Proceedings* (Vol. 9).

643 Cohen, A. S., & Waters, F. G. (1996). Separation of osmium from geological materials by solvent
644 extraction for analysis by thermal ionisation mass spectrometry. *Analytica Chimica*
645 *Acta*, *332*(2-3), 269-275.

646 Day, J.M.D., O'Driscoll, B., Strachan, R.A., Daly, J.S. & Walker, R.J. (2017b) Identification of
647 mantle peridotite as a possible Iapetan ophiolite sliver in south Shetland, Scottish
648 Caledonides. *Journal of the Geological Society of London*, 174, 88-92.

649 Day, J.M.D., Walker, R.J., & Warren, J.M. (2017a). ^{186}Os–^{187}Os and highly siderophile element
650 abundance systematics of the mantle revealed by abyssal peridotites and Os-rich
651 alloys. *Geochimica et Cosmochimica Acta*, *200*, 232-254.

652 Day, J.M.D., Waters, C.L., Schaefer, B.F., Walker, R.J., & Turner, S. (2016b). Use of hydrofluoric
653 acid desilicification in the determination of highly siderophile element abundances and Re-
654 Pt-Os isotope systematics in mafic-ultramafic rocks. *Geostandards and Geoanalytical*
655 *Research*, *40*(1), 49-65.

656 Day, J.M.D., Brandon, A.D., & Walker, R.J. (2016a). Highly siderophile elements in Earth, Mars,
657 the Moon, and asteroids. *Reviews in Mineralogy and Geochemistry*, *81*(1), 161-238.

658 Day, J.M.D., Peters, B.J., & Janney, P.E. (2014). Oxygen isotope systematics of South African
659 olivine melilitites and implications for HIMU mantle reservoirs. *Lithos*, *202*, 76-84.

660 Day, J.M.D., Walker, R.J., Qin, L. and Rumble III, D., 2012. Late accretion as a natural
661 consequence of planetary growth. *Nature Geoscience*, *5*(9), 614-617.

662 DeMets, C., Gordon, R. G., Argus, D. F., & Stein, S. (1990). Current plate motions. *Geophysical*
663 *journal international*, *101*(2), 425-478.

664 Ertel, W., O'Neill, H. S. C., Sylvester, P. J., Dingwell, D. B., & Spettel, B. (2001). The solubility
665 of rhenium in silicate melts: implications for the geochemical properties of rhenium at high
666 temperatures. *Geochimica et Cosmochimica Acta*, *65*(13), 2161-2170.

667 Fischer-Gödde, M., Elfers, B. M., Münker, C., Szilas, K., Maier, W. D., Messling, N., Morishita,
668 T., Van Kranendonk, M. & Smithies, H. (2020). Ruthenium isotope vestige of Earth's pre-
669 late-veneer mantle preserved in Archaean rocks. *Nature*, *579*(7798), 240-244.

670 Fischer-Gödde, M., Becker, H., & Wombacher, F. (2011). Rhodium, gold and other highly
671 siderophile elements in orogenic peridotites and peridotite xenoliths. *Chemical*
672 *Geology*, *280*(3-4), 365-383.

673 Frisby, C., Bizimis, M., & Mallick, S. (2016). Seawater-derived rare earth element addition to
674 abyssal peridotites during serpentinization. *Lithos*, *248*, 432-454.

675 Gale, A., Dalton, C. A., Langmuir, C. H., Su, Y., & Schilling, J. G. (2013). The mean composition
676 of ocean ridge basalts. *Geochemistry, Geophysics, Geosystems*, *14*(3), 489-518.

677 Gannoun, A., Burton, K.W., Day, J.M.D., Harvey, J., Schiano, P. & Parkinson, I. (2016). Highly
678 siderophile element and Os Isotope Systematics of volcanic rocks at divergent and
679 convergent plate boundaries and in intraplate settings. *Reviews in Mineralogy and*
680 *Geochemistry*, 81, 651-724.

681 Haller, M. B., O'Driscoll, B., Day, J.M.D., Daly, J. S., Piccoli, P. M., & Walker, R. J. (2021).
682 Meter-Scale Chemical and Isotopic Heterogeneities in the Oceanic Mantle, Leka Ophiolite
683 Complex, Norway. *Journal of Petrology*, in press.
684 https://doi.org/10.1093/petrology/egab061

685 Harvey, J., Gannoun, A., Burton, K. W., Rogers, N. W., Alard, O., & Parkinson, I. J. (2006).
686 Ancient melt extraction from the oceanic upper mantle revealed by Re–Os isotopes in
687 abyssal peridotites from the Mid-Atlantic ridge. *Earth and Planetary Science*
688 *Letters*, *244*(3-4), 606-621.

689 Hellebrand, E., Snow, J. E., Dick, H. J., & Hofmann, A. W. (2001). Coupled major and trace
690 elements as indicators of the extent of melting in mid-ocean-ridge
691 peridotites. *Nature*, *410*(6829), 677-681.

692 Hoffman, N. R. A., & McKenzie, D. P. (1985). The destruction of geochemical heterogeneities by
693 differential fluid motions during mantle convection. *Geophysical Journal*
694 *International*, *82*(2), 163-206.

695 Holzheid, A., Sylvester, P., O'Neill, H. S. C., Rubie, D. C., & Palme, H. (2000). Evidence for a
696 late chondritic veneer in the Earth's mantle from high-pressure partitioning of palladium
697 and platinum. *Nature*, *406*(6794), 396-399.

698 Hyung, E., & Jacobsen, S. B. (2020). The $^{142}Nd/^{144}Nd$ variations in mantle-derived rocks provide
699 constraints on the stirring rate of the mantle from the Hadean to the present. *Proceedings*
700 *of the National Academy of Sciences*, *117*(26), 14738-14744.

701 Jackson, M. G., Shirey, S. B., Hauri, E. H., Kurz, M. D., & Rizo, H. (2016). Peridotite xenoliths
702 from the Polynesian Austral and Samoa hotspots: Implications for the destruction of
703 ancient ^{187}Os and ^{142}Nd isotopic domains and the preservation of Hadean ^{129}Xe in the
704 modern convecting mantle. *Geochimica et Cosmochimica Acta*, *185*, 21-43.

705 Jagoutz, E., Palme, H., Baddenhausen, H., Blum, K., Cendales, M., Dreibus, G., Spettel, B.,
706 Lorenz, V. & Wänke, H. (1979). The abundances of major, minor and trace elements in
707 the earth's mantle as derived from primitive ultramafic nodules. In *Lunar and Planetary*
708 *Science Conference Proceedings* (Vol. 10, pp. 2031-2050).

709 Jones, J. H., & Drake, M. J. (1986). Geochemical constraints on core formation in the
710 Earth. *Nature*, *322*(6076), 221-228.

711 Kimura, K. A. N., Lewis, R. S., & Anders, E. (1974). Distribution of gold and rhenium between
712 nickel-iron and silicate melts: implications for the abundance of siderophile elements on
713 the Earth and Moon. *Geochimica et Cosmochimica Acta*, *38*(5), 683-701.

714 Klein, F., Bach, W., & McCollom, T. M. (2013). Compositional controls on hydrogen generation
715 during serpentinization of ultramafic rocks. *Lithos*, *178*, 55-69.

716 Lassiter, J. C., Byerly, B. L., Snow, J. E., & Hellebrand, E. (2014). Constraints from Os-isotope
717 variations on the origin of Lena Trough abyssal peridotites and implications for the
718 composition and evolution of the depleted upper mantle. *Earth and Planetary Science*
719 *Letters*, *403*, 178-187.

720 Liu, C. Z., Snow, J. E., Brügmann, G., Hellebrand, E., & Hofmann, A. W. (2009). Non-chondritic
721 HSE budget in Earth's upper mantle evidenced by abyssal peridotites from Gakkel ridge
722 (Arctic Ocean). *Earth and Planetary Science Letters*, *283*(1-4), 122-132.

723 Liu, C. Z., Snow, J. E., Hellebrand, E., Brügmann, G., Von Der Handt, A., Büchl, A., & Hofmann,
724 A. W. (2008). Ancient, highly heterogeneous mantle beneath Gakkel ridge, Arctic
725 Ocean. *Nature*, *452*(7185), 311-316.

726 Lorand, J. P., & Luguet, A. (2016). Chalcophile and siderophile elements in mantle rocks: Trace
727 elements controlled by trace minerals. *Reviews in Mineralogy and Geochemistry*, *81*(1),
728 441-488.

729 Luguet, A., & Pearson, G. (2019). Dating mantle peridotites using Re-Os isotopes: The complex
730 message from whole rocks, base metal sulfides, and platinum group minerals. *American*
731 *Mineralogist: Journal of Earth and Planetary Materials*, *104*(2), 165-189.

732 Luguet, A., & Reisberg, L. (2016). Highly siderophile element and 187Os signatures in non-
733 cratonic basalt-hosted peridotite xenoliths: Unravelling the origin and evolution of the post-
734 Archean lithospheric mantle. *Reviews in Mineralogy and Geochemistry*, *81*(1), 305-367.

735 Luguet, A., Lorand, J. P., & Seyler, M. (2003). Sulfide petrology and highly siderophile element
736 geochemistry of abyssal peridotites: A coupled study of samples from the Kane Fracture
737 Zone (45°W 23°20N, MARK area, Atlantic Ocean). *Geochimica et Cosmochimica*
738 *Acta*, *67*(8), 1553-1570.

739 Luguet, A., Alard, O., Lorand, J. P., Pearson, N. J., Ryan, C., & O'Reilly, S. Y. (2001). Laser-
740 ablation microprobe (LAM)-ICPMS unravels the highly siderophile element geochemistry
741 of the oceanic mantle. *Earth and Planetary Science Letters*, *189*(3-4), 285-294.

742 Maas, C., Manske, L., Wünnemann, K., & Hansen, U. (2021). On the fate of impact-delivered
743 metal in a terrestrial magma ocean. *Earth and Planetary Science Letters*, *554*, 116680.

744 Maier, W.D., Barnes, S.J., Campbell, I.H., Fiorentini, M.L., Peltonen, P., Barnes, S.J. and
745 Smithies, R.H., 2009. Progressive mixing of meteoritic veneer into the early Earth's deep
746 mantle. *Nature*, *460*(7255), pp.620-623

747 Malvoisin, B. (2015). Mass transfer in the oceanic lithosphere: serpentinization is not
748 isochemical. *Earth and Planetary Science Letters*, *430*, 75-85.

749 Marchesi, C., Dale, C. W., Garrido, C. J., Pearson, D. G., Bosch, D., Bodinier, J. L., Gervilla, F.
750 & Hidas, K. (2014). Fractionation of highly siderophile elements in refertilized mantle:
751 Implications for the Os isotope composition of basalts. *Earth and Planetary Science*
752 *Letters*, *400*, 33-44.

753 Marchi, S., Canup, R.M. and Walker, R.J., 2018. Heterogeneous delivery of silicate and metal to
754 the Earth by large planetesimals. *Nature geoscience*, *11*(1), pp.77-81.

755 Martin, C.E. (1991) Osmium isotopic characteristics of mantle-derived rocks. Geochimica et
756 Cosmochimica Acta, 55, 1421-1434.

757 Meisel, T., & Horan, M. F. (2016). Analytical methods for the highly siderophile
758 elements. *Reviews in Mineralogy and Geochemistry*, *81*(1), 89-106.

759 Meisel, T., Walker, R. J., & Morgan, J. W. (1996). The osmium isotopic composition of the Earth's
760 primitive upper mantle. *Nature*, *383*(6600), 517-520.

761 Morgan, J. W. (1986). Ultramafic xenoliths: clues to Earth's late accretionary history. *Journal of*
762 *Geophysical Research: Solid Earth*, *91*(B12), 12375-12387.

763 Morgan, J. W., Walker, R. J., Brandon, A. D., & Horan, M. F. (2001). Siderophile elements in
764 Earth's upper mantle and lunar breccias: data synthesis suggests manifestations of the same
765 late influx. *Meteoritics & Planetary Science*, *36*(9), 1257-1275.

766 Mundl-Petermeier, A., Walker, R. J., Fischer, R. A., Lekic, V., Jackson, M. G., & Kurz, M. D.
767 (2020). Anomalous ^{182}W in high $^{3}He/^{4}He$ ocean island basalts: Fingerprints of Earth's
768 core? *Geochimica et Cosmochimica Acta*, *271*, 194-211.

769 Mundl-Petermeier A., Walker R. J., Jackson M. G., Blichert-Toft J., Kurz M. D. and Halldórsson
770 S. A. (2019) Temporal evolution of primordial tungsten-182 and $^{3}He/^{4}He$ signatures in the
771 Iceland mantle plume. Chem. Geol. 525, 245–259.

772 Mundl, A., Touboul, M., Jackson, M. G., Day, J.M.D., Kurz, M. D., Lekic, V., Helz, R. T. &
773 Walker, R. J. (2017). Tungsten-182 heterogeneity in modern ocean island
774 basalts. *Science*, *356*(6333), 66-69.

775 Murthy, V. R. (1991). Early differentiation of the Earth and the problem of mantle siderophile
776 elements: a new approach. *Science*, *253*(5017), 303-306.

777 Niu, Y. (2004). Bulk-rock major and trace element compositions of abyssal peridotites:
778 implications for mantle melting, melt extraction and post-melting processes beneath mid-
779 ocean ridges. *Journal of Petrology*, *45*(12), 2423-2458.

780 O'Driscoll, B., Walker, R. J., Day, J. M. D., Ash, R. D., & Daly, J. S. (2015). Generations of melt
781 extraction, melt–rock interaction and high-temperature metasomatism preserved in
782 peridotites of the ~497 Ma Leka Ophiolite Complex, Norway. *Journal of Petrology*, *56*(9),
783 1797-1828.

O'Driscoll, B., Day, J. M. D., Walker, R. J., Daly, J. S., McDonough, W. F., & Piccoli, P. M. (2012). Chemical heterogeneity in the upper mantle recorded by peridotites and chromitites from the Shetland Ophiolite Complex, Scotland. *Earth and Planetary Science Letters*, *333*, 226-237.

O'Neill, H. S. C., Dingwell, D. B., Borisov, A., Spettel, B., & Palme, H. (1995). Experimental petrochemistry of some highly siderophile elements at high temperatures, and some implications for core formation and the mantle's early history. *Chemical Geology*, *120*(3-4), 255-273.

Paquet, M., Cannat, M., Brunelli, D., Hamelin, C., & Humler, E. (2016). Effect of melt/mantle interactions on MORB chemistry at the easternmost Southwest Indian Ridge (61°–67° E). *Geochemistry, Geophysics, Geosystems*, *17*(11), 4605-4640.

Parkinson, I. J., Hawkesworth, C. J., & Cohen, A. S. (1998). Ancient mantle in a modern arc: Osmium isotopes in Izu-Bonin-Mariana forearc peridotites. *Science*, *281*(5385), 2011-2013.

Paulick, H., Bach, W., Godard, M., De Hoog, J. C. M., Suhr, G., & Harvey, J. (2006). Geochemistry of abyssal peridotites (Mid-Atlantic Ridge, 15 20′ N, ODP Leg 209): implications for fluid/rock interaction in slow spreading environments. *Chemical Geology*, *234*(3-4), 179-210.

Peters, B. J., Mundl-Petermeier, A., Carlson, R. W., Walker, R. J., & Day, J. M. (2021). Combined Lithophile-Siderophile Isotopic Constraints on Hadean Processes Preserved in Ocean Island Basalt Sources. *Geochemistry, Geophysics, Geosystems*, *22*(3), e2020GC009479.

Peters, B. J., Day, J.M.D., & Taylor, L. A. (2016). Early mantle heterogeneities in the Réunion hotspot source inferred from highly siderophile elements in cumulate xenoliths. *Earth and Planetary Science Letters*, *448*, 150-160.

Rehkämper, M., Halliday, A. N., Fitton, J. G., Lee, D. C., Wieneke, M., & Arndt, N. T. (1999). Ir, Ru, Pt, and Pd in basalts and komatiites: new constraints for the geochemical behavior of the platinum-group elements in the mantle. *Geochimica et Cosmochimica Acta*, *63*(22), 3915-3934.

Reisberg, L. (2021). Osmium isotope constraints on formation and refertilization of the non-cratonic continental mantle lithosphere. *Chemical Geology*, *574*, 120245.

Reisberg, L., & Lorand, J. P. (1995). Longevity of sub-continental mantle lithosphere from osmium isotope systematics in orogenic peridotite massifs. *Nature*, *376*(6536), 159-162.

Ringwood, A. E. (1977). Composition of the core and implications for origin of the Earth. *Geochemical Journal*, *11*(3), 111-135.

Rizo, H., Walker, R. J., Carlson, R. W., Horan, M. F., Mukhopadhyay, S., Manthos, V., ... & Jackson, M. G. (2016). Preservation of Earth-forming events in the tungsten isotopic composition of modern flood basalts. *Science*, *352*(6287), 809-812.

Rouméjon, S. (2014). Serpentinisation des péridotites exhumées aux dorsales lentes : approches microstructurale, minéralogique et géochimique. *Institut de Physique du Globe de Paris.*

Roy-Barman, M., & Allègre, C. J. (1994). $^{187}Os/^{186}Os$ ratios of mid-ocean ridge basalts and abyssal peridotites. *Geochimica et Cosmochimica Acta*, *58*(22), 5043-5054.

825 Sanfilippo, A., Salters, V., Tribuzio, R., & Zanetti, A. (2019). Role of ancient, ultra-depleted
826 mantle in Mid-Ocean-Ridge magmatism. *Earth and Planetary Science Letters*, *511*, 89-98.

827 Schulte, R. F., Schilling, M., Anma, R., Farquhar, J., Horan, M. F., Komiya, T., Farquhar, J.,
828 Piccoli, P. M., Pitcher, L. & Walker, R. J. (2009). Chemical and chronologic complexity
829 in the convecting upper mantle: Evidence from the Taitao ophiolite, southern
830 Chile. *Geochimica et Cosmochimica Acta*, *73*(19), 5793-5819.

831 Seyler, M., Lorand, J. P., Toplis, M. J., & Godard, G. (2004). Asthenospheric metasomatism
832 beneath the mid-ocean ridge: Evidence from depleted abyssal peridotites. *Geology*, *32*(4),
833 301-304.

834 Seyler, M., Cannat, M., & Mével, C. (2003). Evidence for major-element heterogeneity in the
835 mantle source of abyssal peridotites from the Southwest Indian Ridge (52° to
836 68°E). *Geochemistry, Geophysics, Geosystems*, *4*(2).

837 Sichel, S.E., Esperanca, S., Motoki, A., Maia M., Horan, M.F., Szatmari, P., da Costa Alves, E.,
838 Mello, S.L.M. (2008). Geophysical and geochemical evidence for cold upper mantle
839 beneath the equatorial Atlantic Ocean. Revista Brasileira de Geofisica, 26, 69-86.

840 Snortum, E., Day, J.M.D. (2020) Forearc origin for Coast Range Ophiolites inferred from osmium
841 isotopes and highly siderophile elements. Chemical Geology, 550, 119723.

842 Snortum, E., Day, J.M.D., & Jackson, M. G. (2019). Pacific lithosphere evolution inferred from
843 Aitutaki mantle xenoliths. *Journal of Petrology*, *60*(9), 1753-1772.

844 Snow, J.E., & Dick, H.J. (1995). Pervasive magnesium loss by marine weathering of
845 peridotite. *Geochimica et Cosmochimica Acta*, *59*(20), 4219-4236.

846 Snow, J. E., & Reisberg, L. (1995). Os isotopic systematics of the MORB mantle: results from
847 altered abyssal peridotites. *Earth and Planetary Science Letters*, *133*(3-4), 411-421.

848 Snow, J. E., & Schmidt, G. (1998). Constraints on Earth accretion deduced from noble metals in
849 the oceanic mantle. *Nature*, *391*(6663), 166-169.

850 Standish, J.J., Hart, S.R., Blusztajn, J., Dick, H.J.B., Lee, K.L. (2002) Abyssal peridotite osmium
851 isotopic compositions from Cr-spinel. Geochemistry, Geophysics, Geosystems, 3,
852 10.1029/2001GC000161.

853 Stracke, A., Snow, J. E., Hellebrand, E., von der Handt, A., Bourdon, B., Birbaum, K., & Günther,
854 D. (2011). Abyssal peridotite Hf isotopes identify extreme mantle depletion. *Earth and*
855 *Planetary Science Letters*, *308*(3-4), 359-368.

856 Suer, T.-A., Siebert, J., Remusat, L., Day, J.M.D., Borensztajn, S., Doisineau, B., Fiquet, G. (2021)
857 Reconciling metal-silicate partitioning and late accretion in the Earth. Nature
858 Communications. 12, 2193. https://doi.org/10.1038/s41467-021-23137-5.

859 Turekian, K. K., & Clark Jr, S. P. (1969). Inhomogeneous accumulation of the Earth from the
860 primitive solar nebula. *Earth and Planetary Science Letters*, *6*(5), 346-348.

861 Van de Löcht, J., Hoffmann, J. E., Li, C., Wang, Z., Becker, H., Rosing, M. T., Münker, C. (2018).
862 Earth's oldest mantle peridotites show entire record of late accretion. *Geology*, *46*(3), 199-
863 202.

Walker, R. J., Carlson, R. W., Shirey, S. B., & Boyd, F. R. (1989). Os, Sr, Nd, and Pb isotope systematics of southern African peridotite xenoliths: implications for the chemical evolution of subcontinental mantle. *Geochimica et Cosmochimica Acta*, *53*(7), 1583-1595.

Wänke, H. (1981). Constitution of terrestrial planets. *Philosophical Transactions of the Royal Society of London. Series A, Mathematical and Physical Sciences*, *303*(1477), 287-302.

Warren, J. M. (2016). Global variations in abyssal peridotite compositions. *Lithos*, *248*, 193-219.

Warren, J. M., Shimizu, N., Sakaguchi, C., Dick, H. J. B., & Nakamura, E. (2009). An assessment of upper mantle heterogeneity based on abyssal peridotite isotopic compositions. *Journal of Geophysical Research: Solid Earth*, *114*(B12).

Waterton, P., Mungall, J., & Pearson, D. G. (2021). The komatiite-mantle platinum-group element paradox. *Geochimica et Cosmochimica Acta*.

Willbold, M., Elliott, T., & Moorbath, S. (2011). The tungsten isotopic composition of the Earth's mantle before the terminal bombardment. *Nature*, *477*(7363), 195-198.

Zhang, C., Liu, C. Z., Ji, W. B., Liu, T., & Wu, F. Y. (2020). Heterogeneous sub-ridge mantle of the Neo-Tethys: Constraints from Re-Os isotope and HSE compositions of the Xigaze ophiolites. *Lithos*, 105819.

881 **TABLE CAPTIONS**

882 **Table 1.** Osmium isotope and highly siderophile element abundance (ppb) data in abyssal
883 peridotites.

884 **Tables S1 to S7.** Ancillary, major, trace element and the available published HSE and Os isotope
885 dataset for abyssal peridotites. Accuracy and precision for standard reference materials and total
886 procedural blanks are provided for isotope dilution HSE abundance analyses.

887

FIGURES & FIGURE CAPTIONS

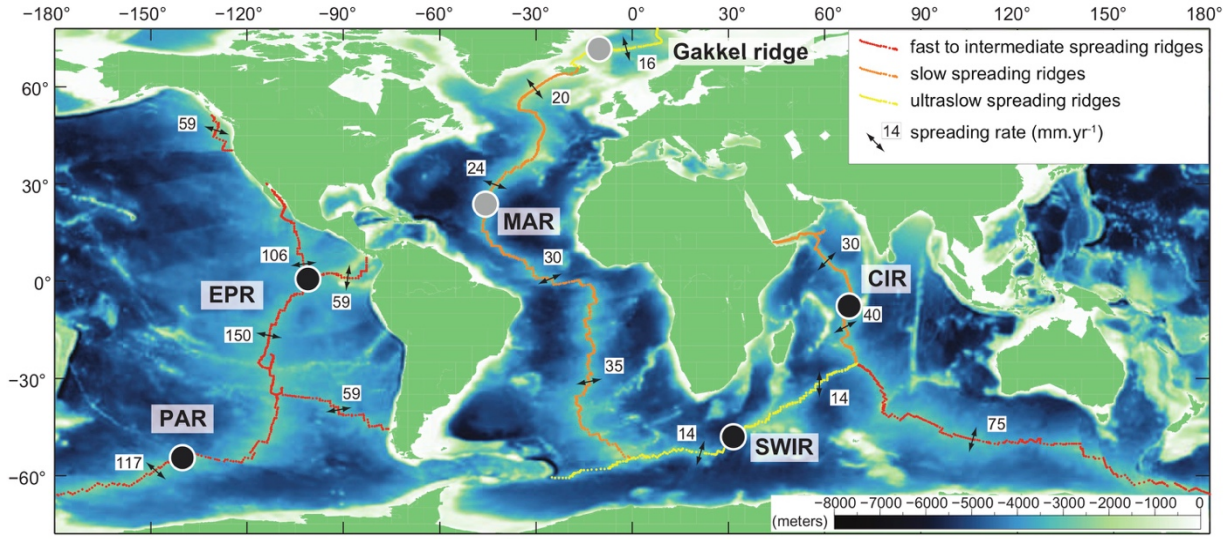

Figure 1. Mid-ocean ridge full spreading rates and the location of abyssal peridotites analyzed for Re-Os isotopes and HSE abundance systematics in this study (EPR, PAR, SWIR, CIR) and prior studies (modified from Rouméjon, 2014). Spreading rates are from DeMets et al. (1990). The black circles represent locations of new HSE and Os isotope data for abyssal peridotites from Hess Deep along the East Pacific Rise (EPR) and from the Udintsev fracture zone along the Pacific Antarctic Ridge (PAR), as well as from the Central and Southwest Indian Ridges. The light gray circles correspond to abyssal peridotite samples from other slower spreading centers (Snow and Schmidt, 1998; Brandon et al., 2000, 2006; Luguet et al., 2001, 2003; Becker et al., 2006; Liu et al., 2009; Lassiter et al., 2014; Day et al., 2017a; Li et al., 2019).

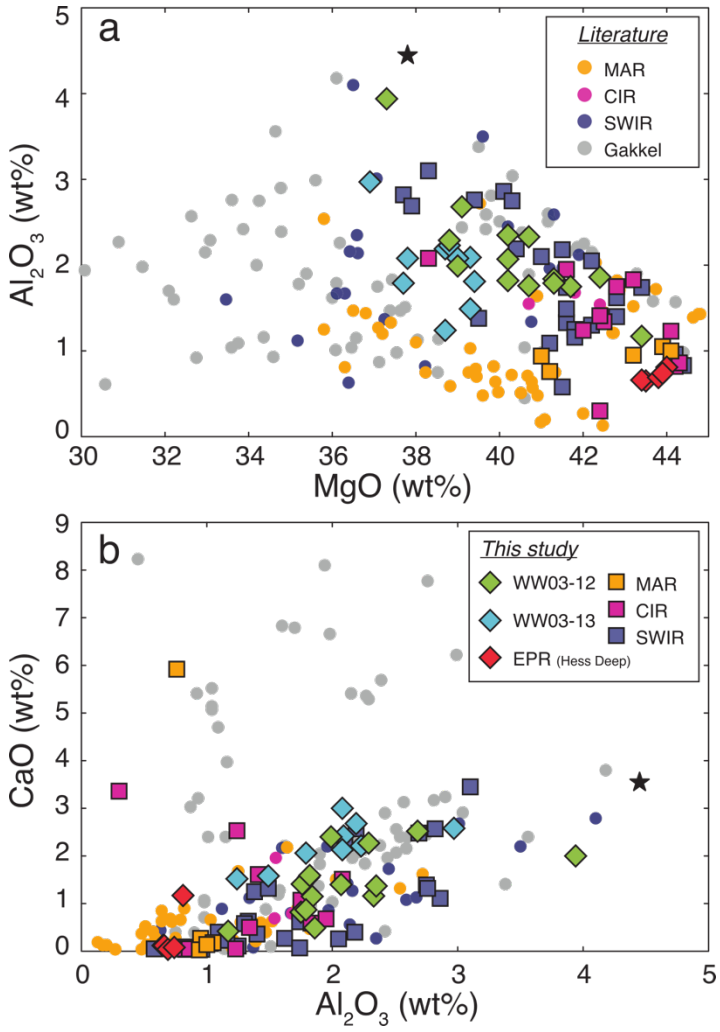

899

900 **Figure 2.** Variations (in wt.%) of (a) Al_2O_3 as a function of MgO and (b) CaO as a function of
901 Al_2O_3 for bulk rock abyssal peridotites from the dredges WEST03MV-12 and WEST03MV-13
902 (abbreviated WW03-12 and WW03-13 respectively) along the Pacific Antarctic Ridge, Hess Deep
903 region along the East Pacific Rise, the Southwest Indian Ridge, the Central Indian Ridge and the
904 Mid-Atlantic Ridge. Also shown for comparison are abyssal peridotites from the Gakkel ridge, the
905 Southwest Indian Ridge, the Central Indian Ridge and the Mid-Atlantic Ridge for which HSE and
906 Os isotope data are available (see Table S7 for references). The star corresponds to the Primitive
907 Mantle estimate from McDonough and Sun (1995). (For interpretation of the references to color
908 in this figure legend, the reader is referred to the web version of this article).

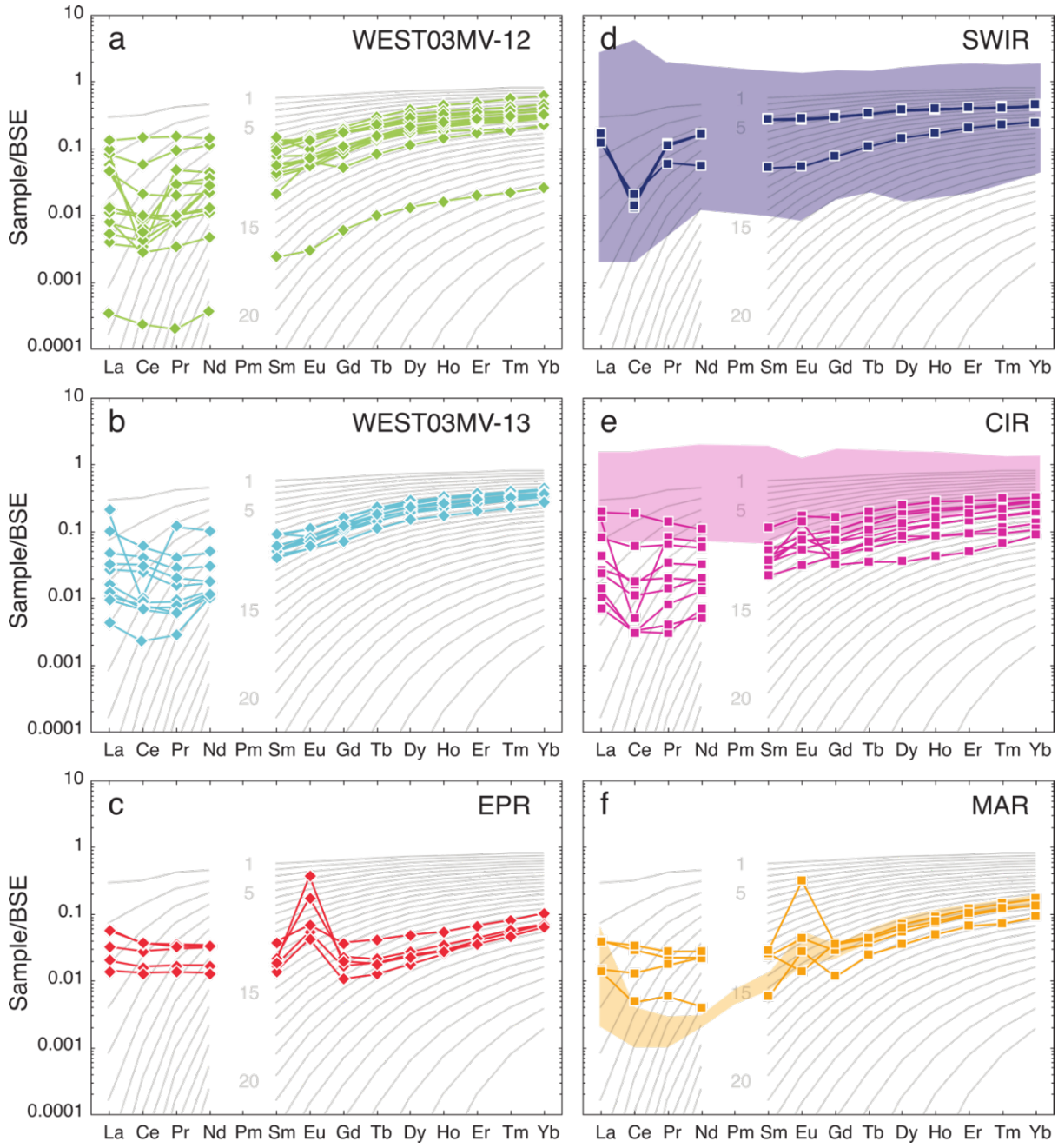

Figure 3. Bulk Silicate Earth-normalized rare earth element (REE) concentrations in abyssal peridotites from the dredges WEST03MV-12 (a) and WEST03MV-13 (b) along the Pacific Antarctic Ridge (PAR), Hess Deep region along the East Pacific Rise (EPR) (c), SWIR (d), CIR (e) and MAR (f). Shaded fields are abyssal peridotites from Day et al., (2017a). Normalizing values from McDonough & Sun (1995). Gray lines represent 1% melt increments for a non-modal fractional melting model (see Day et al., 2017a for model parameters). An increase of melt depletion is associated with lower absolute REE abundances and higher depletion in the LREE relative to the HREE.

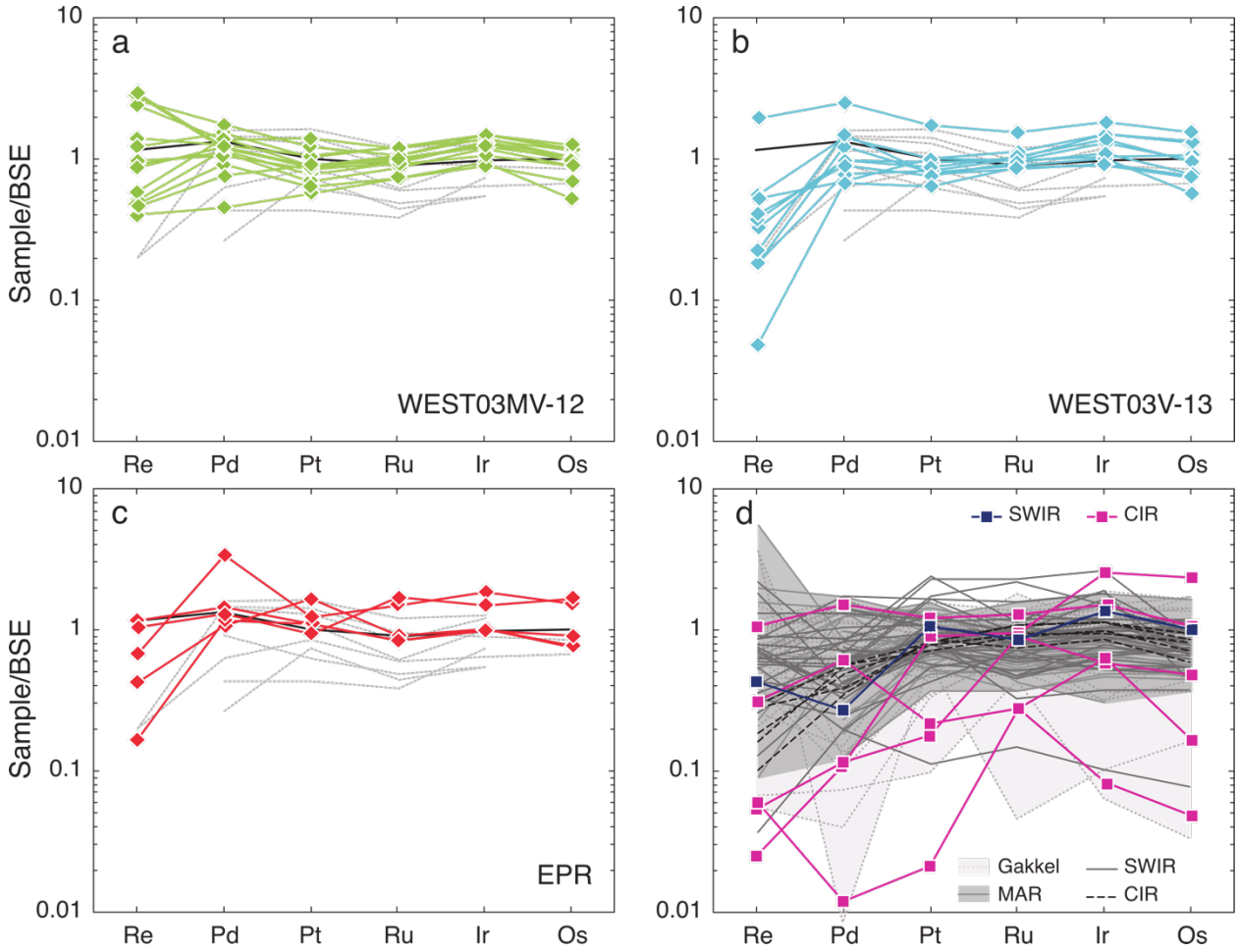

Figure 4. Bulk Silicate Earth-normalized HSE concentrations in abyssal peridotites from the dredges WEST03MV-12 (a) and WEST03MV-13 (b) along the Pacific Antarctic Ridge (PAR), Hess Deep region along the East Pacific Rise (EPR) (c), SWIR and CIR, together with slow-spreading ridge abyssal peridotite literature data as comparison (Brandon et al., 2000: Liu et al., 2009; Lassiter et al., 2014; Day et al., 2017a; Li et al., 2019) (d). Normalizing values from Day et al. (2017a). Gray dashed lines correspond to previous studies on Hess Deep abyssal peridotites (Snow & Schmidt, 1998; Rehkämper et al.,1999). The black solid line in panels a-c corresponds to the Primitive Upper Mantle (PUM) estimate from Becker et al. (2006).

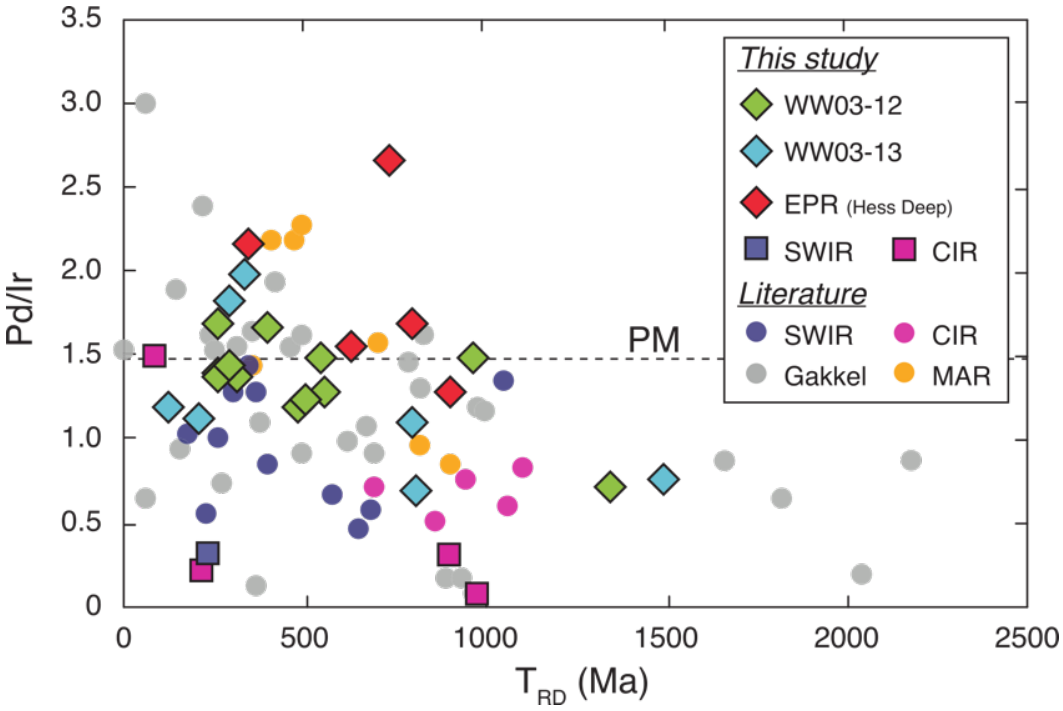

927

928 **Figure 5.** Time of Re depletion model ages (T_{RD}) versus Pd/Ir. Primitive mantle (also referred to
929 as BSE) Pd/Ir is from Day et al. (2017a). Literature data are from Snow and Schmidt (1998),
930 Becker et al., 2006, Liu et al. (2008, 2009), and Day et al. (2017a). (For interpretation of the
931 references to color in this figure legend, the reader is referred to the web version of this article).

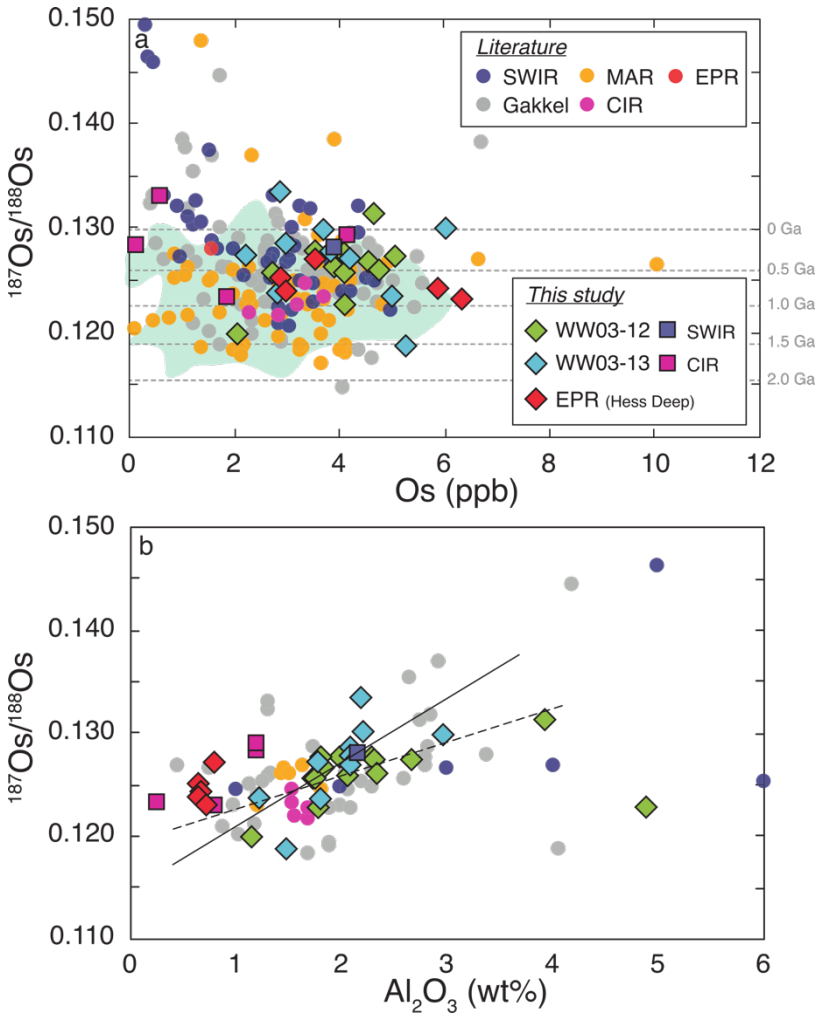

Figure 6. Relationship between $^{187}Os/^{188}Os$ ratios and (a) Os and (b) Al_2O_3 contents in abyssal peridotites. The dashed and solid lines correspond to the linear regression for the WEST03MV-12 (r^2 = 0.64) and WEST03MV-13 peridotites (r^2 = 0.5), respectively. Literature data for abyssal peridotites are given in the text and can be found in Supplementary Table 7. The green field represents the peridotite xenoliths from the Pacific Ocean (Bizimis et al., 2007; Jackson et al., 2016; Snortum et al., 2019). The dotted grey lines are the depletion ages for a BSE composition. (For interpretation of the references to color in this figure legend, the reader is referred to the web version of this article).

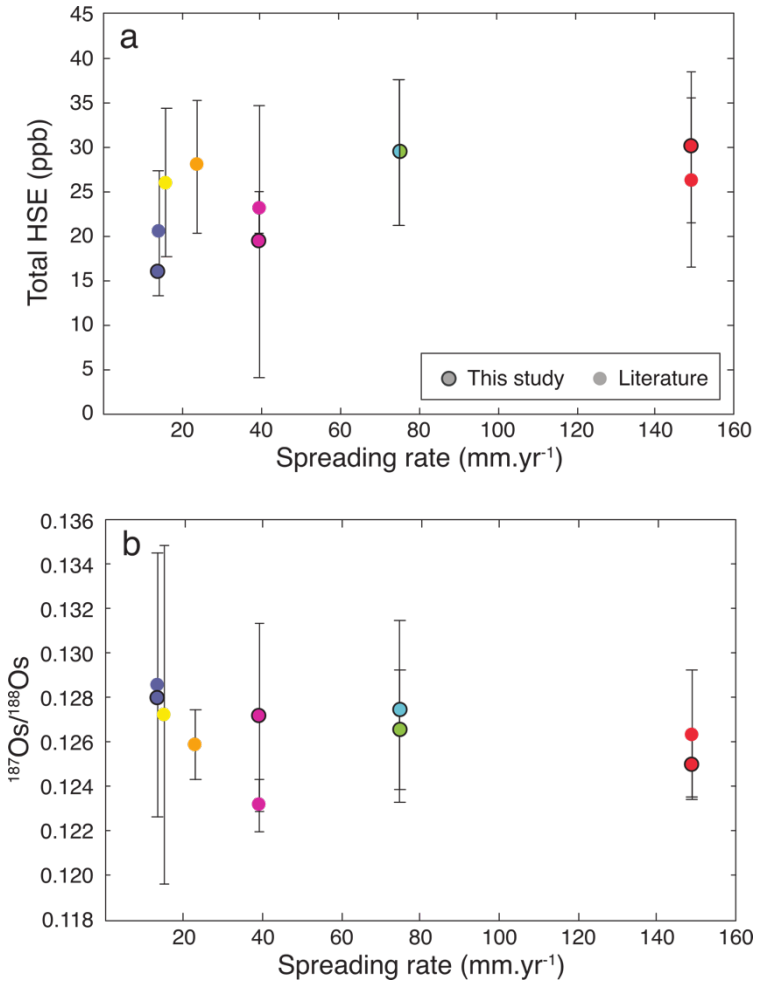

942

943 **Figure 7.** Average (a) total HSE contents in ppb, and (b) $^{187}Os/^{188}Os$ ratios as a function of
944 spreading rate. Spreading rates are as reported in Figure 1.

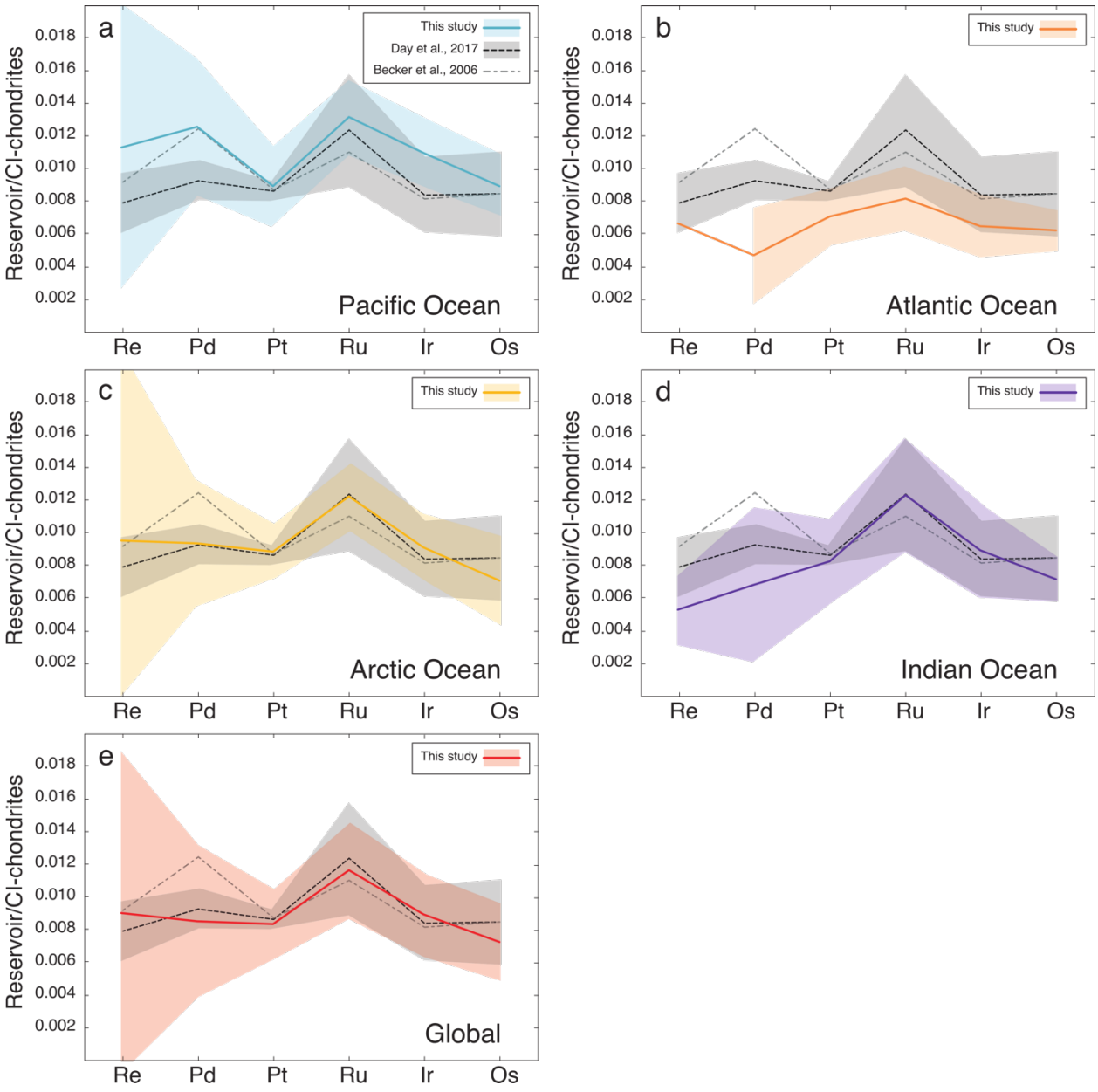

945

946 **Figure 8.** Estimates for the mantle composition for each ocean basin (solid lines), considered to
947 be represented by abyssal peridotites with Al_2O_3 > 2 wt.% (this study; Brandon et al., 2000: Liu et
948 al., 2009; Lassiter et al., 2014; Day et al., 2017a; Li et al., 2019) (a) Pacific Ocean, (b) Atlantic
949 Ocean, (c) Arctic Ocean, (d) Indian Ocean and (e) for the global abyssal peridotite sample suite.
950 Colored fields correspond to the standard deviation of the calculated mantle composition. Dashed
951 lines correspond to the primitive (upper) mantle estimates from Becker et al., (2006) and Day et
952 al. (2017a). The grey field represents the 2 SD uncertainty of the estimate from Day et al. (2017a).
953 Note that abyssal peridotites from the CIR and Hess Deep along the EPR were not included in the
954 calculation for the Indian and Pacific oceans due to their low Al_2O_3 content. (For interpretation of
955 the references to color in this figure legend, the reader is referred to the web version of this article).